Conformations of *N*-Acetyl-L-Prolinamide by Two-Dimensional Infrared Spectroscopy[†]

Soohwan Sul, Denis Karaiskaj,[‡] Ying Jiang, and Nien-Hui Ge*

Department of Chemistry, University of California, Irvine, California 92697-2025

Received: April 2, 2006; In Final Form: August 16, 2006

Femtosecond two-dimensional infrared (2D IR) spectroscopy has been applied to study the conformations of a model dipeptide, *N*-acetyl-L-prolinamide (AcProNH$_2$) in deuterated chloroform (CDCl$_3$). Spectral features in the amide-I and -II regions are obtained by rephasing (R), nonrephasing (NR), and reverse photon echo (RPE) pulse sequences with two polarization conditions. The 2D spectra obtained by the RPE and NR sequences with (0, 0, 0, 0) polarization reveal new spectral features associated with the multiple conformers of AcProNH$_2$ that are difficult to discern using R sequence and linear-IR spectroscopy. The high resolving power of the RPE sequence comes from destructive interference between the positive and negative peaks of nearby vibrators, similar to the NR sequence. The RPE response functions that are useful for 2D spectral simulations are evaluated, including the effects of vibrational frequency correlations. The 2D spectra obtained with (45, −45, 90, 0) polarization exhibit clear cross-peak patterns in the off-diagonal region for the R and RPE sequences but in the diagonal region for the NR sequence. These patterns, free from strong diagonal contributions, are crucial for structure determination. DFT calculations, normal-mode analysis, Hessian matrix reconstruction, and vibrational exciton Hamiltonian diagonalization yield molecular parameters needed for quantitative simulations of 2D spectra: angles between transition dipoles, coupling constants, and off-diagonal anharmonicities of the amide-I and -II modes are obtained for solvated *trans*-C$_7$ and cis structures and for gas-phase trans conformers in the region of $\phi = -120°$ to $0°$ and $\psi = -100°$ to $180°$ in the Ramachandran space. Systematic simulations based on a 4:1 population ratio of the solvated *trans*-C$_7$ and cis structures reproduce well the 2D spectral features obtained at both polarization conditions. However, better agreement between the experimental and simulated cross-peak patterns can be reached if the dihedral angles of the major trans conformer are close to $(\phi, \psi) = (-80°, 100°)$. Our results suggest that the major conformer of AcProNH$_2$ in CDCl$_3$ deviates from the gas-phase global minimum, the *trans*-C$_7$ form, to an extended intermediate between the C$_7$ and polyproline-II structure. These results are discussed in relationship with earlier findings obtained by NMR, transient IR studies, and MD simulations.

1. Introduction

Terminally blocked amino acids and dipeptides have long served as the primary models for theoretical and experimental studies of backbone conformations in peptides and proteins. Among these model systems, *N*-acetyl-L-prolinamide (AcPro-NH$_2$)[1–13] and its derivatives have received much attention because the unique five-membered ring on the proline residue has been shown to have significant effects on chain conformations[14] and the process of protein folding.[15,16] Earlier studies on AcProNH$_2$[1,2,4–6] and its *N'*-methyl derivative (AcPro-NHMe)[1,5,17–20] using optical rotatory dispersion, circular dichroism, NMR, FT-IR, and theoretical calculations suggested that the structure of this proline dipeptide is of the trans and cis forms and their relative populations depend on several factors such as temperature, concentration, and solvent polarity. In the gas phase and nonpolar solvents, the internally hydrogen-bonded *trans*-C$_7$ structure (C$_7$, also called the γ-turn) is most stable (Figure 1a), whereas in polar solvents, the trans right-handed α-helix (α_R) (Figure 1b), *trans*-polyproline II (P$_{II}$) (Figure 1c), and cis conformations (Figure 1d) become increasingly popu-

lated.[5] More recently, ultrafast vibrational spectroscopies[7–10] on AcProNH$_2$ observed spectral features that were attributed to the presence of multiple conformations in aqueous and nonpolar solvents, but the assignment of conformations was at variance with one another. Two-dimensional infrared (2D IR) spectroscopic studies by Zanni et al. using the rephasing (R) sequence[7,8] suggested that two conformers coexist in chloroform. The earlier study suggests that one conformer is close to an α_R and the other to an intermediate between the C$_5$ and P$_{II}$ structures,[7] while in the latter study, one conformer is like C$_5$ and the other like C$_7$.[8] On the basis of transient anisotropy measurements, Rubtsov and Hochstrasser concluded that AcProNH$_2$ in dichloromethane (CH$_2$Cl$_2$) adopts a C$_7$ form in the presence of a minor α_R structure.[10] Stimulated by these experimental results, Hahn et al. performed ab initio calculations and MD simulations on the trans conformation. Their results showed that the C$_7$ structure is the most stable form in vacuo, but the ensemble-averaged structure in CDCl$_3$ takes a different form ($\phi = -70°$ and $\psi = 15°$).[11] The discrepancies regarding the conformations of this model dipeptide clearly point to the need for further experimental and theoretical investigations.

Recent developments in 2D IR spectroscopy[21–30] have provided new ways to explore the structure and dynamics of peptides and proteins.[7,31–44] 2D IR is a vibrational analogue to 2D NMR spectroscopy, but with far better (subpicosecond) time
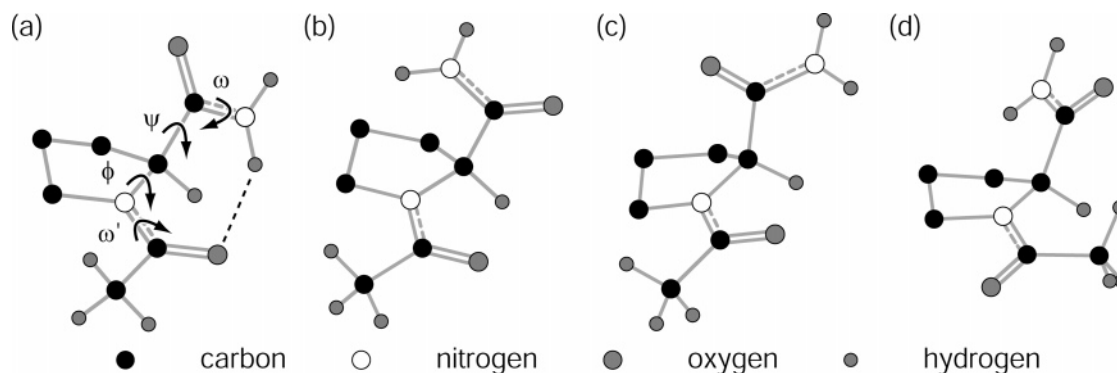
Figure 1. Chemical diagram of AcProNH$_2$ and the pertinent dihedral angles that define its conformation. (a) The *trans*-C$_7$ form (also called the γ-turn) of AcProNH$_2$ is presented with dihedral angles, $(\omega', \phi, \psi, \omega) = (-172°, -84°, 65°, -178°)$. A seven-membered ring (C$_7$) forms by an intramolecular hydrogen bond between the acetyl CO and amino NH group (dashed line). Other trans forms have different ψ angles but a similar ϕ angle due to the ring constraint. The trans right-handed α-helix (α_R) form with $\psi = -50°$ (b) and the *trans*-polyproline II (P$_{II}$) form with $\psi = 150°$ (c) are also presented. (d) The cis conformer differs mainly in ω' and ψ, with dihedral angles, $(\omega', \phi, \psi, \omega) = (9°, -88°, -10°, -180°)$. For clarity, only backbone hydrogen atoms are shown.

resolution. For short oligopeptides that undergo picosecond to nanosecond conformational fluctuations,[33,45,46] 2D IR has the potential to reveal new structural information that is hard to access by 2D NMR due to conformational averaging. In a typical 2D IR spectrum, diagonal peaks provide information about individual vibrators, whereas cross-peaks mirror the strength of the couplings between different vibrators. Because the coupling arises from through-bond and through-space interactions between vibrational modes, the coupling strength acutely depends on the underlying molecular structure. By conducting 2D IR experiments using polarized light, information on the transition dipole orientation can be extracted from the cross-peak intensities and anisotropies,[7,32,42] and such angle information has been used to infer the structure of peptide backbones. The results from these initial 2D IR studies appeared very promising. However, a recent theoretical study questioned the ability of cross-peak anisotropy measurements in providing quantitatively reliable angles when the cross-peaks are not well resolved from the diagonal peaks.[11] For most peptides studied to date, including AcProNH$_2$ in water and chloroform,[7-9,11,47] the diagonal features are broad enough to affect the accuracy of cross-peak anisotropy measurements. It is therefore necessary to devise a different 2D IR approach to circumvent this problem.

In this paper, we present an extensive study of the amide-I and -II modes of AcProNH$_2$ in CDCl$_3$ using three 2D IR pulse sequences at two polarization conditions. Our strategy is to obtain a large set of 2D spectral constraints for unique dynamics and structure determination. Because of the different pulse ordering employed in the rephasing (R), nonrephasing (NR), and reverse photon echo (RPE) sequences, the resulting 2D spectra are quite different in the diagonal and cross-peak positions and in their dependence on vibrational frequency inhomogeneity and correlations. These properties are explored at an all-parallel polarization condition to resolve the closely spaced spectral features resulting from multiple conformers and to determine the vibrational dynamics parameters. We overcome the problem of spectral congestion using a double-crossed polarization configuration that is capable of suppressing the diagonal peaks. The revealed cross-peak patterns are shown to be crucial for structure determination. The combination of quantum chemical and semiempirical calculations with extensive 2D IR spectral simulations allows us to determine the ensemble-averaged structure of AcProNH$_2$.

2. Experimental Setup and Methods

2.1. Mid-IR 2D Spectrometer. The mid-IR pulses were generated by difference frequency mixing of the signal and idler outputs of a home-built optical parametric amplifier (OPA)[48] pumped by a commercial ultrafast regenerative amplified Ti: sapphire laser system (Spectra Physics). The pulses from the Ti:sapphire amplifier are at 800 nm with ~95 fs duration and a repetition rate of 1 kHz. The white-light seeded two-stage BBO (type-II, 4 mm thickness) OPA is pumped (total 320 mW) with ~5 μJ in the first pass and 300 μJ in the second pass and generates signal and idler pulses between 1.2 and 2.3 μm. Difference frequency mixing in a 0.5 mm thick type-I AgGaS$_2$ crystal generates IR pulses of ~100 fs duration, with a bandwidth of 170 cm^{-1} and about 1 μJ of energy at 6 μm. The IR radiation is collimated to a diameter of 6 mm by a curved mirror and filtered by a germanium long pass filter.

The IR output is split into three beams of wavevectors k_a, k_b, and k_c, each with 300 nJ, and a local oscillator beam k_{LO}, of 30 nJ, using ZnSe beam splitters (Rocky Mountain Instrument). The three excitation pulses and the local oscillator pulse traverse computer-controlled linear motor translation stages (Aerotech, ALS130), which set the time delays between them. The three input beams are focused on the sample in box geometry using a 100 mm focal length off-axis parabolic mirror (Janos Technologies). The four-wave mixing signal generated at the phase matching direction $k_s = -k_a + k_b + k_c$ is collimated by a second off-axis parabolic mirror and collinearly combined with the attenuated local oscillator beam using a one-sided AR-coated ZnSe beam splitter and is focused onto a liquid nitrogen cooled single-element HgCdTe detector (Infrared Associates). A chopper blocks the k_a beam at 500 Hz and allows the intensity solely from the local oscillator beam to be subtracted.

The polarization of all the excitation beams is controlled using MgF$_2$ zero-order half-wave plates (Karl Lambrecht) followed by BaF$_2$ wire-grid polarizers (Specac) placed immediately in front of the first focusing parabolic mirror before the sample. The polarization of the generated field is selected using a polarizer placed immediately after the sample, which is set to be the same as the polarizer placed in the local oscillator beam. All mirrors in the interferometer have bare-gold coating to minimize the ellipticity of polarization. Polarization conditions used in this paper are listed in the order of (p_a, p_b, p_c, p_s), where p_n refers to the polarization of the excitation pulses, or the signal field, with a wave vector k_n. The polarization angle is expressed

Conformations of *N*-Acetyl-L-Prolinamide

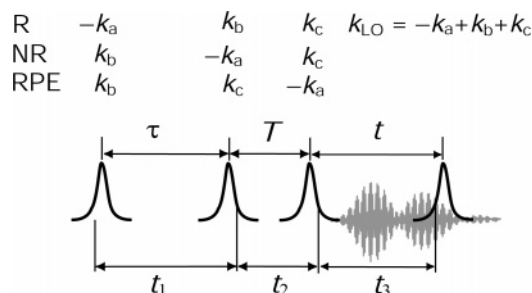*J. Phys. Chem. B, Vol. 110, No. 40, 2006* **19893**

Figure 2. Schematic diagram of the three pulse sequences used in the experiments: rephasing (R), nonrephasing (NR), and reverse photon echo (RPE). Three IR pulses with different wave vectors k_a, k_b, and k_c arrive at the sample with the time intervals denoted by τ and T. Another IR pulse, k_{LO}, heterodynes the signal with time delay, t, at the phase-matching direction $-k_a + k_b + k_c$.

in degrees with $p_n = 0$ referring to vertical (i.e. s-) polarization in the laboratory frame.

Figure 2 illustrates the three pulse sequences used in the experiments: The time ordering between the three excitation pulses is a−b−c, b−a−c, and b−c−a for the R, NR, and RPE sequences, respectively. The three sequences at a single phase-matching angle give rise to signals equivalent to those generated by a single sequence in three phase-matching directions.[49,50] The time intervals between the first and second pulses, between the second and third pulses, and between the third and local oscillator pulses are denoted as τ, T, and t, respectively. Nonresonant, third-order solvent response detected at the same phase-matching direction was used to determine time zero between excitation and local oscillator pulses. For the R and NR sequences, τ was scanned from 0 to 2500 fs in 18 fs steps, T was set to zero, and t was scanned from 0 to 2500 fs in 18 fs steps. In the RPE sequence, τ was set to zero, T was scanned from 0 to 900 fs in 9 fs steps, and t was scanned from 0 to 2500 fs in 18 fs steps. The 2D IR spectra $\underline{S}_R(-\omega_\tau, T, \omega_t)$, $\underline{S}_{NR}(\omega_\tau, T, \omega_t)$, and $\underline{S}_{RPE}(\tau, \omega_T, \omega_t)$ were obtained by performing 2D Fourier transform of the heterodyne signal $S(\tau, T, t)$ along the two scanning time axes. To remove the nonresonant solvent contributions, data points within the first 150 fs of the τ and T scans were deleted from the acquired data before signal processing. For a fixed τ or T position, the intensity of the homodyne signal results in a small constant contribution to the total signal intensity along each t scan. This contribution was removed before performing Fourier transform.

Heterodyne transient grating signals were measured by setting the time ordering between the three excitation pulses to a−b−c. τ was set to zero, T was scanned from −2 ps to 14 ps in 75 fs steps, and t was scanned from 0 to 2500 fs in 18 fs steps. The signal processing procedure is the same as the above except that 1D Fourier transform along the t axis was performed to obtain $\underline{S}(0, T, \omega_t)$.

Pump−probe spectra were obtained by measuring the difference in transmission of the k_b beam when the sample was pumped by the k_a beam that was chopped at 500 Hz. The probe beam intensity was reduced by a factor of 10 for these measurements. Broad-band detection of the probe pulses was achieved by a 64-channel MCT array (Infrared Associates) with matching electronics (Infrared Systems Development). The array is mounted on the focal plane of a 300 mm spectrograph (Acton) with a 75 *l*/mm grating, resulting in a spectral resolution of 2.2 cm^{-1} per channel at 6 μm.

2.2. Sample Preparation. AcProNH$_2$ was purchased from Bachem and used without further purification. Deuterated chloroform (CDCl$_3$, 99.96% D) was purchased from Cambridge
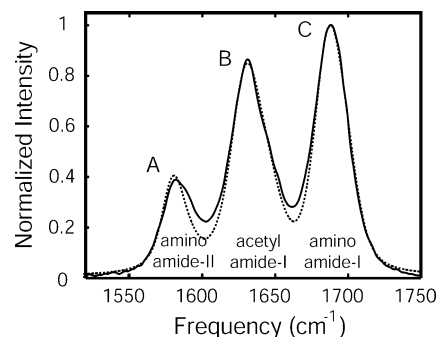

Figure 3. FT-IR spectra of AcProNH$_2$ in CDCl$_3$. The background spectrum of the neat solvent was subtracted. Peak A corresponds to the amide-II band of the amino end, peak B corresponds to the amide-I band of the acetyl end, and peak C corresponds to the amide-I band of the amino end. The dotted line is from the simulation discussed in Section 4.6.

Isotope Laboratories, Inc. The sample was a 110 mM solution of AcProNH$_2$ in CDCl$_3$ held between two 2 mm thick CaF$_2$ windows with a 25 μm spacer. All experiments were performed at ambient temperature 20.1 ± 0.3 °C.

3. Results

3.1 Linear-IR Spectrum. The linear FT-IR spectrum of AcProNH$_2$ in CDCl$_3$ is shown in Figure 3. It has three absorption bands; an amide-II band of the amino end (A, 1583 cm^{-1}), and two amide-I bands of the acetyl and amino ends (B, 1632 cm^{-1}, and C, 1689 cm^{-1}, respectively). The spectrum was least-squares fitted to three Voigt profiles. The integrated areas give absorption intensities of 140, 550, and 470 km/mol for peaks A, B, and C, respectively, and yield corresponding transition dipoles of magnitude 1.8, 3.6, and 3.3 DÅ^{-1} amu$^{-1/2}$. The amide-I band transition dipoles are close to the experimental value reported for the same peptide in CH$_2$Cl$_2$ (0.33 D for peak B)[10] and to the theoretical value of 3.7 DÅ^{-1} amu$^{-1/2}$ previously derived.[51] Figure 3 also shows a simulated spectrum (dotted line) based on a theoretical model that will be discussed in detail later in Section 4.6.

3.2. The 2D IR Spectra. The absolute magnitude 2D IR spectra acquired using the R, NR, and RPE sequences at (0, 0, 0, 0) polarization are shown in Figure 4a$_1$−a$_3$. The diagonal peaks are labeled by A, B, and C, corresponding with those in the FT-IR spectrum in Figure 3. The cross-peaks are labeled as D, E, and F. Here, we have chosen to denote cross-peaks arising from the same pair of diagonal peaks by a single label: two D peaks result from couplings between peaks A and B, E peaks from A and C, and F peaks from B and C.

The diagonal peaks in the R spectrum (Figure 4a$_1$) are line-narrowed along the antidiagonal, but not in the NR spectrum (Figure 4a$_2$). The diagonal peak intensities in the R versus NR spectra exhibit a ∼4:1 ratio for both peaks B and C, and a ∼1.4:1 ratio for peak A. The differences in the line shape between the R and NR spectra and the intensity ratios indicate the presence of inhomogeneous distributions.[9,52] The diagonal peaks in the RPE spectrum (Figure 4a$_3$) appear at the overtone and combination band frequencies and are elongated along the ω_T dimension, indicating that the dephasing of the 0−2 coherences is faster than that of the 0−1 coherences.

Parts c$_1$−c$_3$ of Figure 4 present the diagonal slices (red) through the most intense peak in the 2D IR spectra. While the diagonal profile of the amide-I bands in the R spectrum contains two smooth peaks, the B and C bands in the NR and RPE spectra exhibit shoulders at the higher frequency sides of the main peaks.
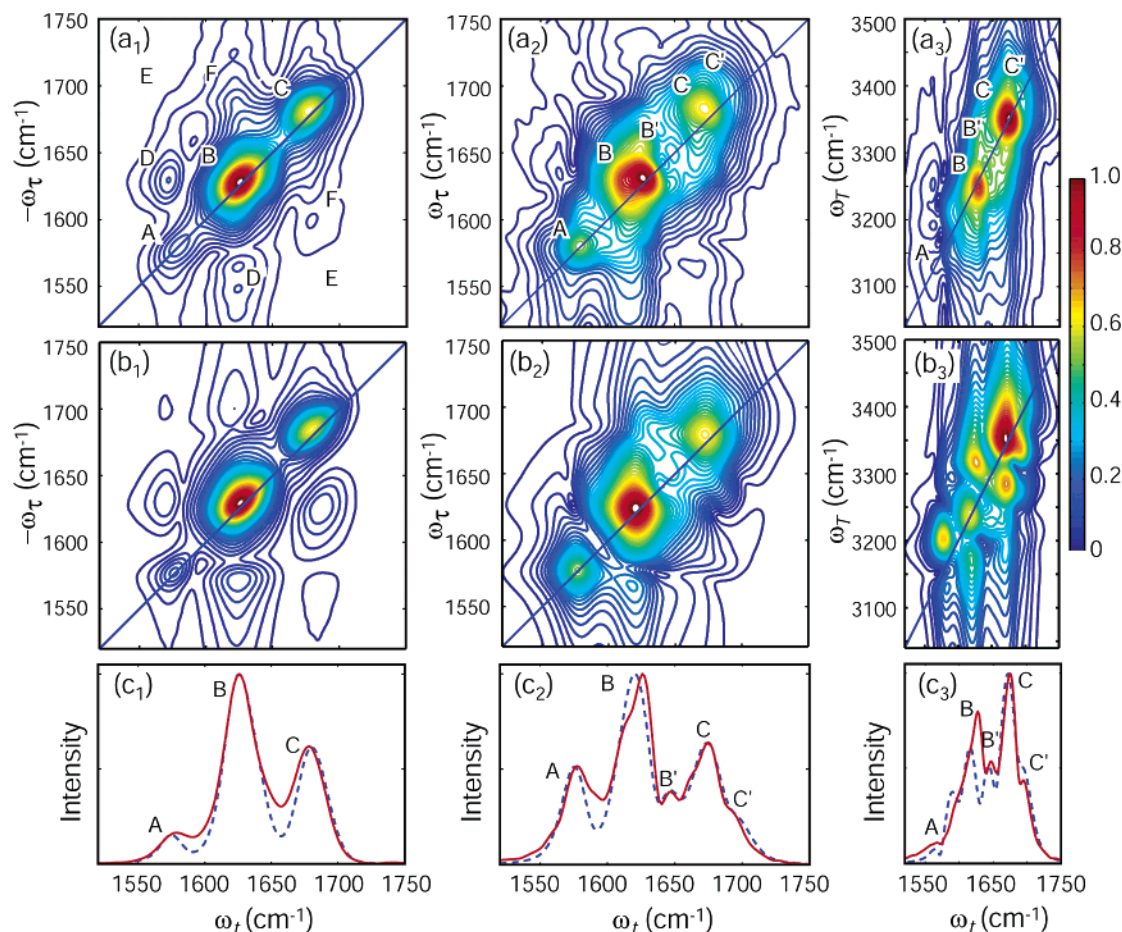
Figure 4. Absolute magnitude 2D IR spectra of AcProNH$_2$ in CDCl$_3$ and their simulations at the (0, 0, 0, 0) polarization condition. Experimental spectra $|S_R(-\omega_\tau, 0, \omega_t)|$, $|S_{NR}(\omega_\tau, 0, \omega_t)|$, and $|S_{RPE}(0, \omega_T, \omega_t)|$ are arranged in panels (a$_1$), (a$_2$), and (a$_3$), respectively. The corresponding simulations based on a 4:1 population ratio of the solvated *trans*-C$_7$ and cis conformers are arranged in the second row below each spectrum (b$_1$–b$_3$). Diagonal slices of 2D IR spectra through the highest peak maximum from experiments (solid red) and simulations (dashed blue) are shown in the third row (c$_1$–c$_3$). Doublet features labeled as B and B′ and C and C′ are resolved in the NR and RPE spectra. The central frequencies of the pulses are 1600, 1600, and 1640 cm^{-1} for R, NR, and RPE, respectively. The spectra were normalized and plotted using 40 evenly spaced contour lines.

Therefore, both amide-I bands consist of at least two subbands. The elongation of the peaks along the diagonal in the R spectrum and the presence of doublet features in the NR and RPE spectra indicate that AcProNH$_2$ has more than one conformation in CDCl$_3$ and the separation of amide-I frequencies of the conformers is less than their line widths. In comparison to the linear spectrum in Figure 3, the 2D IR slices in Figure 4c$_2$ and c$_3$ show clearly resolved minor components, labeled as B′ and C′, and provide explicit evidence for the existence of multiple conformers.

The R spectrum (Figure 4a$_1$) shows three sets of cross-peaks, D, E (very weak), and F, in contrast to previous studies where six cross-peaks in the upper off-diagonal region were observed.[7,8] This is attributed to the different data acquisition and treatment procedures used in the present study. We collected longer time scans and did not process data using window functions.

Parts a$_1$–a$_3$ of Figure 5 show the R, NR, and RPE spectra taken at (45, −45, 90, 0) polarization. In the R spectrum (Figure 5a$_1$), E cross-peaks become most intense, although they are almost invisible at (0, 0, 0, 0) polarization. D peaks are clearly seen, but F peaks remain very weak. In the RPE spectrum (Figure 5a$_3$), D and E peaks are also strong. However, in the NR spectrum (Figure 5a$_2$), we see dominating spectral features located along the diagonal, but not in the off-diagonal region. This behavior is because cross-peaks in the off-diagonal regions are suppressed at this polarization condition (see Section 4.3).

Although the features in the 1650–1700 cm^{-1} region appear weak, they are reproducible.

3.3. Pump–Probe Spectra. The pump/probe experiments were performed at three center wavelengths (1600, 1630, and 1660 cm^{-1}) at a pump–probe delay of 200 fs. At this time delay, the pulses do not overlap, so the distortion of pump–probe spectra due to solvent response can be neglected. These spectra, together with the FT-IR spectrum, were simultaneously least-squares fitted to six Voigt functions. Three of them, at the fundamental frequencies, were used to describe the linear absorption as well as the pump–probe ground-state bleaches plus stimulated emissions of $v = 1 \rightarrow 0$. The other three, at the anharmonically shifted frequencies, described the excited-state absorptions $v = 1 \rightarrow 2$. The diagonal anharmonicities were determined to be 10.7, 11.0, and 12.4 cm^{-1} for the A, B, and C peaks, respectively. The ratio of the areas of the excited-state absorption and the ground-state bleach is proportional to the ratio of the squared transition dipole moments for the $v = 1 \rightarrow 2$ and $v = 0 \rightarrow 1$ transitions. From the fits, ratios of 2.9, 2.0, and 1.7 were found for the A, B, and C peaks, respectively. These ratios indicate that the amide-I vibrators are nearly harmonic. The line widths of the bleach are 23, 32, and 27 cm^{-1} for the A, B, and C peaks, respectively. The line width of the corresponding absorption is similar to that of the bleach to within 1–2 cm^{-1}. Figure 6 shows one of the pump–probe spectra
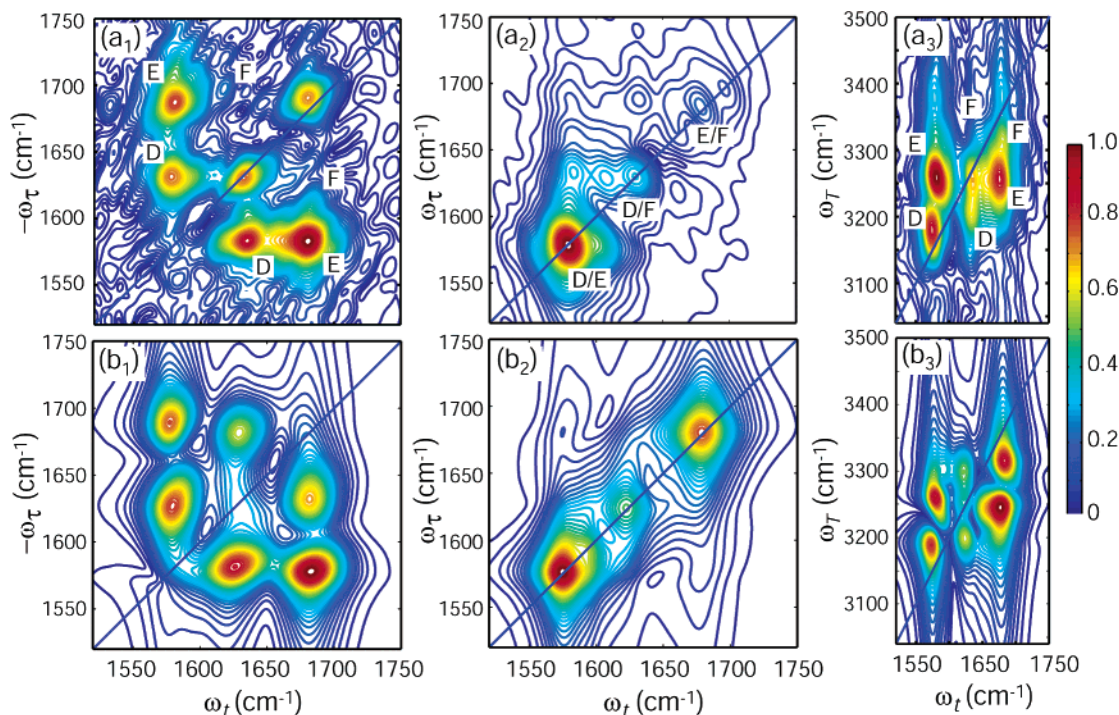
Figure 5. Absolute magnitude 2D IR spectra of AcProNH$_2$ in CDCl$_3$ and their simulations at the (45, −45, 90, 0) polarization condition. Experimental spectra $|\underline{S}_R(-\omega_\tau, 0, \omega_t)|$, $|\underline{S}_{NR}(\omega_\tau, 0, \omega_t)|$, and $|\underline{S}_{RPE}(0, \omega_T, \omega_t)|$ are arranged in panels (a$_1$), (a$_2$), and (a$_3$), respectively. Simulations based on a 4:1 population ratio of the solvated *trans*-C$_7$ and cis conformers are arranged in the second row below each spectrum (b$_1$−b$_3$). For all three experimental spectra, the E cross-peaks are the most intense. All three simulated spectra show similar cross-peak patterns to the experimental data, except that F peaks are too strong. The central frequencies of IR pulses are 1600 cm^{-1} for all three spectra. The spectra are normalized and plotted using 40 evenly spaced contour lines.
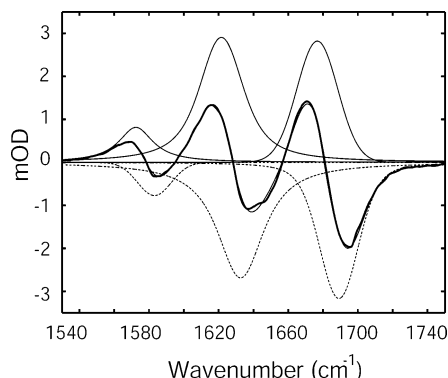

Figure 6. Broad-band-pump/broad-band-probe spectrum (thick line) of AcProNH$_2$ in CDCl$_3$ and the fit (thin line). The pulses have a central frequency of 1600 cm^{-1} and a pump−probe delay of 200 fs. Also shown are the six Voigt functions used in the fit: three negative peaks at the fundamental frequencies (dashed) and three positive peaks at anharmonically shifted $v = 1 \rightarrow 2$ transition frequencies (solid).

together with the fits. The presence of a second conformer is clearly seen from the splitting of the ground-state bleach of the B peak.

3.4. Heterodyne Transient Grating. The population relaxation time of the $v = 1$ states were measured by means of heterodyne transient grating signals. Figure 7 shows plots of $|\underline{S}(0, T, \omega_t)|$ versus T at three different values of ω_t. The decay of the signal along the T-axis is determined by the loss of population of the $v = 1$ state or any intermediate state generated from the $v = 1$ state that can couple with the k_c pulse. The decay curves in Figure 7 were fitted with double exponential decays that were convolved with a Gaussian instrument response. The parameters are quoted in the caption of Figure 7. The dominating faster decay is considered here to be the actual T_1 lifetime. The slower decay is attributed to arise from

rotational relaxation or from populational relaxation of states that were not originally excited.

4. Discussion

Section 4.1 outlines a theoretical formalism to provide guidelines for interpretation and simulation of 2D IR spectra. Section 4.2 details the effects of the (45, −45, 90, 0) polarization condition on 2D IR spectra. In Section 4.3, we discuss the origin of the high resolving power of the RPE sequence and perform a model calculation for two nearby vibrators. In Section 4.4, we present the results from conformational analysis and normal-mode calculations on AcProNH$_2$ in vacuo and in chloroform. Section 4.5 introduces an extended Hessian matrix reconstruction method to obtain the coupling constants of coupled amide-I and -II vibrators, followed by diagonalization of two-exciton Hamiltonian that provides the diagonal and off-diagonal anharmonicities. Finally, simulations of 2D IR spectra are presented and comments on the conformations of AcProNH$_2$ in CDCl$_3$ are made in Sections 4.6 and 4.7, respectively.

4.1. Response Functions and Descriptions of 2D Spectra. The principles governing the R, NR, and RPE contributions to the 2D IR spectra of coupled vibrators have been described previously[9,49,50,53] and are briefly summarized here to provide guidelines for the following spectral interpretation. For a multiple vibrator system, the third-order response of the system is a sum of the individual responses from the eight Feynman diagrams shown in Figure 8. Here we label the fundamental states of the *i*th and *j*th vibrator as i and j with frequencies ω_i and ω_j, respectively. The two quantum states are labeled as k, where the overtone state of the *i*th vibrator is $k = i + i$ with frequency $\omega_{i+i} = 2\omega_i - \Delta_{ii}$, and the combination band state of the *i*th and *j*th vibrators is $k = i + j$, with frequencies $\omega_{i+j} = \omega_i + \omega_j - \Delta_{ij}$. The diagonal and off-diagonal anharmonicities are denoted by Δ_{ii} and Δ_{ij}, respectively. These eight diagrams
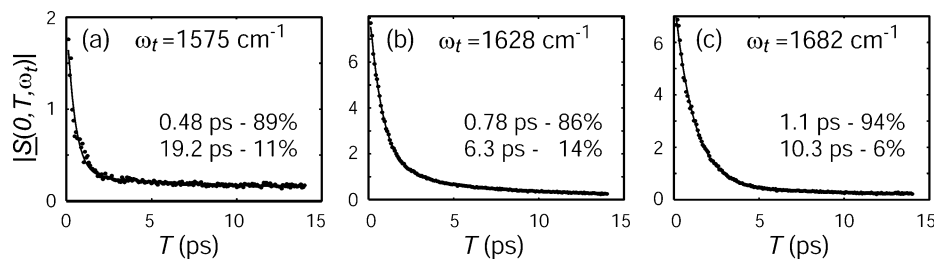
Figure 7. Heterodyned transient grating signals $|\underline{S}(0, T, \omega_t)|$ at specific ω_t. The solid lines are fits to a biexponential decay function $A_1 \exp(-T/\tau_1)$ $+ A_2 \exp(-T/\tau2)$. The parameters are (a) $\omega_t = 1575$ cm^{-1}, $A_1 = 1.82$, $\tau_1 = 0.48$ ps, $A_2 = 0.23$, $\tau_2 = 19.2$ ps; (b) $\omega_t = 1628$ cm^{-1}, $A_1 = 7.42$, $\tau_1 = 0.78$ ps, $A_2 = 1.25$, $\tau_2 = 6.3$ ps; (c) $\omega_t = 1682$ cm^{-1}, $A_1 = 7.24$, $\tau_1 = 1.1$ ps, $A_2 = 0.49$, $\tau_2 = 10.3$ ps. The dominating decay is considered here as the actual T_1 lifetime.

can be broken into three sets: 1−3, 4−6, and 7−8, which produce the responses of the R, NR, and RPE sequences, respectively.

In the case of impulsive excitation, the time intervals τ, T, and t between the centers of the pulses are the same as the time intervals t_1, t_2, and t_3 between excitations (Figure 2). The complex response functions generated from the eight diagrams can be expressed by

$$\mathscr{R}_R(\tau, T, t) = \sum_{i \neq j} \{\langle\alpha_i\beta_i\gamma_i\delta_i\rangle[\mathscr{T}_b(0i|00|i0) + \mathscr{T}_b(0i|ii|i0) -$$
$$\mathscr{T}_a(0i|ii|i+i,i)] + \langle\alpha_i\beta_i\gamma_j\delta_j\rangle[\mathscr{T}_d(0i|00|j0) -$$
$$\mathscr{T}_c(0i|ii|i+j,i)] + \langle\alpha_i\beta_j\gamma_i\delta_j\rangle[\mathscr{T}_d(0i|ji|j0) -$$
$$\mathscr{T}_c(0i|ji|i+j,i)] - \langle\alpha_i\beta_j\gamma_i\delta_j\rangle\mathscr{T}_e(0i|ii|j+j,i) -$$
$$\langle\alpha_i\beta_j\gamma_j\delta_f\rangle\mathscr{T}_e(0i|ji|j+j,i) - \langle\alpha_i\beta_j\gamma_j\delta_i\rangle\mathscr{T}_a(0i|ji|i+i,i)\} \quad (1)$$

$$\mathscr{R}_{NR}(\tau, T, t) = \sum_{i \neq j} \{\langle\alpha_i\beta_i\gamma_i\delta_i\rangle[\mathscr{T}_b(i0|00|i0) +$$
$$\mathscr{T}_b(i0|ii|i0) - \mathscr{T}_a(i0|ii|i+i,i)] +$$
$$\langle\alpha_i\beta_i\gamma_j\delta_j\rangle[\mathscr{T}_d(i0|00|j0) - \mathscr{T}_c(i0|ii|i+j,i)] +$$
$$\langle\alpha_i\beta_j\gamma_j\delta_i\rangle[\mathscr{T}_b(i0|ij|i0) - \mathscr{T}_g(i0|ij|i+j,j)] -$$
$$\langle\alpha_i\beta_i\gamma_j\delta_f\rangle\mathscr{T}_e(i0|ii|j+j,i) - \langle\alpha_i\beta_j\gamma_j\delta_f\rangle\mathscr{T}_m(i0|ij|i+i,j) -$$
$$\langle\alpha_i\beta_j\gamma_j\delta_j\rangle\mathscr{T}_n(i0|ij|j+j,j)\} \quad (2)$$

$$\mathscr{R}_{RPE}(\tau, T, t) = \sum_{i \neq j} \{\langle\alpha_i\beta_i\gamma_i\delta_i\rangle[\mathscr{T}_b(i0|i+i,0|i0) -$$
$$\mathscr{T}_a(i0|i+i,0|i+i,i)] + \langle\alpha_i\beta_j\gamma_i\delta_j\rangle[\mathscr{T}_d(i0|i+j,0|j0) -$$
$$\mathscr{T}_c(i0|i+j,0|i+j,i)] + \langle\alpha_i\beta_j\gamma_i\delta_i\rangle[\mathscr{T}_h(i0|i+j,0|i0) -$$
$$\mathscr{T}_g(i0|i+j,0|i+j,j)] + \langle\alpha_i\beta_i\gamma_j\delta_j\rangle\mathscr{T}_n(i0|i+i,0|j0) -$$
$$\langle\alpha_i\beta_i\gamma_j\delta_f\rangle\mathscr{T}_m(i0|i+i,0|i+i,j) +$$
$$\langle\alpha_i\beta_j\gamma_j\delta_i\rangle\mathscr{T}_s(i0|j+j,0|i0) -$$
$$\langle\alpha_i\beta_f\gamma_j\delta_j\rangle\mathscr{T}_e(i0|j+j,0|j+j,i) +$$
$$\langle\alpha_i\beta_f\gamma_j\delta_j\rangle\mathscr{T}_q(i0|j+j,0|j0) -$$
$$\langle\alpha_i\beta_f\gamma_j\delta_j\rangle\mathscr{T}_p(i0|j+j,0|j+j,j)\} \quad (3)$$

In these equations, it has been assumed that orientational dynamics and vibrational dynamics are independent of each other. The factors $\langle\alpha_m\beta_n\gamma_u\delta_w\rangle$ denote the ensemble averaged products of the projections of the angles of the m, n, u, and w transition dipoles in the molecular frame onto the polarization directions of the laser pulses α, β, γ, and signal field δ in the laboratory frame. Transitions that are forbidden in the harmonic and extreme weak coupling limit are labeled with "*f*" and the angles of these transition dipoles depend on the details of how the oscillators are coupled. The factors $\langle\alpha_m\beta_n\gamma_u\delta_w\rangle$ can include orientational diffusions or internal motions of transition dipoles during the time of pulse excitations. Manipulation of these factors through laser polarizations allows for enhancement and

suppression of specific peaks in 2D spectra.[8,53−55] The vibrational dynamics and time evolution of the system are contained in the factors $\mathscr{F}(mn|qr|uw) = F(mn|qr|uw) \exp[i(\omega_m - \omega_n)\tau$ $+ i(\omega_q - \omega_r)T + i(\omega_u - \omega_w)t]$, where $\hbar\omega_m$ is the energy of the state m involved in the transition. The factors $F(mn|qr|uw)$ can include population relaxation as well as vibrational and rotational dephasing, which are responsible for two-dimensional line shapes in 2D spectra. These factors also include the product of the transition dipoles involved in the Feynman path, which determines the peak intensities. Additional response functions are necessary to account for population and coherence transfer, which are neglected here. The explicit forms of $F(mn|qr|uw)$ for the RPE sequence including correlations effects are derived in the Appendix. The corresponding equations for the R and NR sequences have been reported previously.[9]

Parts a−c of Figure 8 schematically illustrate the 2D IR spectra as a result of these response functions for two coupled vibrators i and j. Each $\mathscr{F}$ term in eqs 1−3 is labeled with the corresponding subscript together with the preceding sign in Figure 8. Several $\mathscr{F}$ paths that are labeled with the same subscript produce peaks at the same positions in the 2D spectra. For the R sequence (Figure 8a), the peaks appear in the quadrants where ω_τ and ω_t are of the opposite sign. The real part of the 2D spectra is expected to show two pairs of diagonal peaks (blue) and two pairs of cross-peaks (pink). The diagonal peaks are due to successive light interactions with the same vibrators. They are located at the fundamental frequencies along the $-\omega_\tau$ dimension, and each pair contains a positive ($\mathscr{T}_b$'s) and a negative ($\mathscr{T}_a$) part that are separated by the diagonal anharmonicity along the ω_t dimension. The cross-peaks result from successive light interactions with two coupled vibrators. They are located in the off-diagonal regions and the splitting between the positive ($\mathscr{T}_d$'s) and negative ($\mathscr{T}_c$'s) parts corresponds to the off-diagonal anharmonicity.

For the NR sequence (Figure 8b), the phase of the initial coherence generated by the first pulse is not reversed by the third pulse. The peaks appear in the quadrants where ω_τ and ω_t are of the same sign. Different from the R spectrum where two sets of cross-peaks are located at the same frequencies, the NR spectrum has one set of cross-peaks ($\mathscr{T}_c$ and $\mathscr{T}_d$) located in the off-diagonal region with the other set of cross-peaks ($\mathscr{T}_b$ and $\mathscr{T}_g$) located along the diagonal, overlapping with the diagonal peaks.

In contrast to the R and NR sequences, two successive excitations in the RPE sequence create a two-quantum coherence during the T period. Therefore, the RPE spectrum (Figure 8c) has two pairs of diagonal peaks at the overtone frequencies along the ω_T dimension and two pairs of cross-peaks at the combination band frequencies. If the peak positions are determined accurately, the RPE sequence allows direct measurements of the diagonal and off-diagonal anharmonicities.[53] The off-diagonal anharmonicity is a very important parameter because it is related to the coupling constant between the vibrational

Conformations of *N*-Acetyl-L-Prolinamide

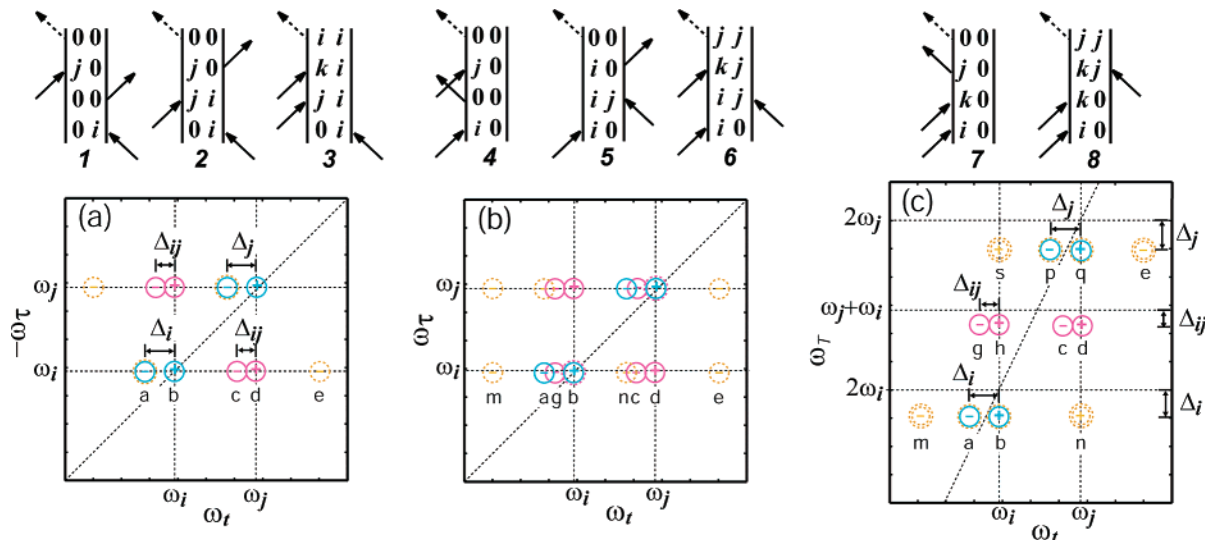*J. Phys. Chem. B, Vol. 110, No. 40, 2006* **19897**

Figure 8. Feynman diagrams contributing to the third-order nonlinear signals and the real part of the 2D IR spectra for two weakly coupled vibrators *i* and *j* for R (a), NR (b), and RPE (c) sequences. The peaks resulting from Liouville paths that excite vibrator *i* during the first laser pulse interaction are labeled a−s, corresponding to the subscript of $\mathcal{F}$ in eqs 1−3. The $\mathcal{F}$ paths with the same subscript produce peaks at the same positions in the 2D IR spectrum. Diagonal peaks, cross-peaks, and "forbidden" peaks are represented by blue, pink, and orange circles, respectively.

TABLE 1: $\langle \alpha_m \beta_n \gamma_u \delta_w \rangle$ Factors for Polarization $(p_a, p_b, p_c, p_s) = (45, -45, 90, 0)$ Assuming a Spherical or Rodlike Diffuser with a Diffusion Coefficient D^a

mnuw	R a−b−c	NR b−a−c	RPE b−c−a	R a−c−b	NR b−c−a	RPE c−b−a
iiii	0	0	$\frac{1}{18}(1 - e^{-6DT}) \equiv K$	$-K$	K	K
iijj	0	0				L
ijij	$\frac{1}{18}(P_2 - 1)e^{-2DT} \equiv L$		$\frac{1}{54}(1 + 2P_2) - \frac{1}{108}(5 + P_2)e^{-6DT} + \frac{1}{36}(1 - P_2)e^{-2DT} \equiv M$	$-M$	M	N
ijji		L	$\frac{1}{54}(1 + 2P_2) - \frac{1}{108}(5 + P_2)e^{-6DT} - \frac{1}{36}(1 - P_2)e^{-2DT} \equiv N$		N	M

^{a} The *m*, *n*, *u*, and *w* transition dipoles interact with laser pulses in a sequence generating diagonal (*iiii*) and cross peaks (*iijj*, *ijij*, and *ijji*). Overlapping laser pulses for each pulse sequence (R, b−c; NR, a−c; RPE, b−c) produce two different angular factors depending on the temporal order of the excitation photons. A common factor, $e^{-2D(\tau + t)}$, is omitted

modes, which in turn is related to the molecular structure. A recent theoretical study suggests that the RPE signal is more sensitive to the coupling than the R signal.[56] In terms of dynamical parameters, the dephasing rate of the two quantum states can be directly measured during the *T* period. The dynamical information of these states is important for quantitative simulation of 2D spectra in general. Similar to the NR sequence, the RPE sequence is also "nonrephased" and the peaks appear in the quadrants where ω_T and ω_t are of the same sign.

4.2. The (45, −45, 90, 0) Polarization Condition. The general expression for angular factors $\langle \alpha_m \beta_n \gamma_u \delta_w \rangle$ for an arbitrary set of transition dipoles in an isotropic media has been reported previously.[54] By selecting the polarization (p_a, p_b, p_c, p_s) of the excitation pulses and the four-wave mixing signal, the contribution of diagrams 1−8 to the diagonal or cross-peaks can be strategically manipulated. In this paper, we employed the (0, 0, 0, 0) and (45, −45, 90, 0) polarization conditions. Table 1 lists a complete set of $\langle \alpha_m \beta_n \gamma_u \delta_w \rangle$ factors for the (45, −45, 90, 0) polarization condition for a spherical or rodlike diffuser with diffusion coefficient *D*. All permutations of pulse ordering that occur during pulse overlap are considered. Experimental applications of this polarization has been demonstrated in the R[8,57] and RPE[53] sequences. Here we apply it to all three sequences simultaneously and show that the NR sequence exhibits quite different behavior from the R and RPE sequences.

A couple of points should be noted in Table 1. First, when *T* is very small and/or systems have slow rotational diffusion, the exponential factors e^{-6DT} and e^{-2DT} are essentially 1, and the *K*, *L*, *M*, and *N* terms become close to 0, $(P_2 - 1)/18$, 0, and $(P_2 - 1)/18$, respectively, where $P_2 = (3\cos^2\theta_{ij} - 1)/2$ and θ_{ij} is

the angle between transition dipoles of vibrational modes *i* and *j*. The diagonal peaks (*iiii*) in the R, NR, and RPE are completely suppressed. One set of cross-peaks (*iijj* for the R and NR, and *ijij* for the RPE) is suppressed, while the other set of cross-peaks (*ijij* for the R, and *ijji* for the NR and RPE) survives if $P_2 \neq 1$. For the R and RPE sequences, the surviving sets of cross-peaks are located in off-diagonal regions, and therefore, only off-diagonal features will remain in the corresponding 2D IR spectra. On the contrary, the off-diagonal cross-peaks ($\mathcal{F}_c$ and $\mathcal{F}_d$ in Figure 8b) are suppressed for the NR sequence, and hence, its 2D IR spectrum will only contain cross-peaks along the diagonal ($\mathcal{F}_b$ and $\mathcal{F}_g$).

Second, when rotational diffusion is fast and *T* is nonzero, the *K* term will give rise to diagonal contributions to the 2D spectra and the *M* term will give rise to cross-peak contributions. To minimize the undesired diagonal contributions in the R and NR sequences, one can set a well-separated time delay between the second and third excitation pulses to include contributions only from the a−b−c and b−a−c pulse ordering. In comparison to the R and NR sequences, the RPE sequence at this polarization is more susceptible to the diagonal contributions from the *K* term because *T* is scanned and thus, not zero. The cross-peak contributions from the *M* term will appear in the off-diagonal region for all three sequences, and thus the NR spectrum will exhibit off-diagonal cross-peaks in this case.

The behavior predicted by Table 1 is observed in the experimental spectra for AcProNH$_2$ in Figure 5a$_1$−a$_3$. Because the R and NR spectra were obtained at $T = 0$ and the measured rotational diffusion time of AcProNH$_2$ in CH$_2$Cl$_2$ is 8−10 ps,[10] the first case described above should apply. The diagonal features in the R and RPE spectra are largely suppressed as
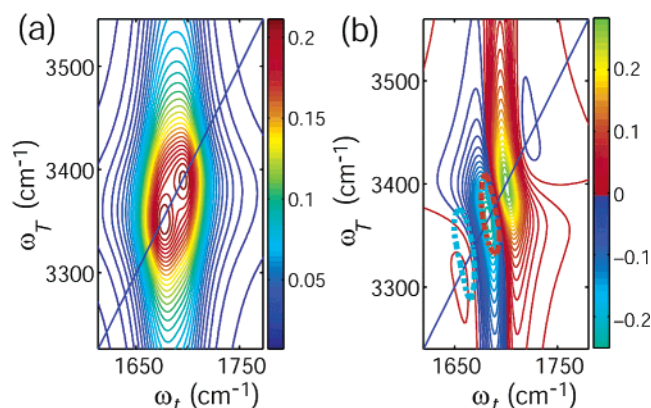
Figure 9. (a) Calculated absolute magnitude 2D RPE spectrum for two closely spaced independent vibrators at $\omega_i^0 = 1700$ cm^{-1} and $\omega_j^0 = 1686$ cm^{-1} with identical dynamical parameters $\Gamma_i = 6.4$ cm^{-1}, and $\sigma_i = 6.0$ cm^{-1}, and $f_i = 0$. (b) The real part of 2D RPE spectrum for the vibrator at $\omega_i^0 = 1700$ cm^{-1}. To illustrate the effect of interference between two vibrators, the spectrum for the other vibrator at $\omega_i^0 = 1686$ cm^{-1} is shown schematically by a pair of positive and negative ellipses (dashed lines). See Figure 6 in ref 9 for the effects of overlapping vibrators on R and NR spectra.

compared to those at the (0, 0, 0, 0) polarization condition in Figure 4a$_1$ and a$_3$. The off-diagonal cross-peaks are clearly seen in the R and RPE spectra, but they are diminished in the NR spectrum at (45, −45, 90, 0) polarization. The main spectral features in the NR spectrum are along the diagonal. In principle, the coupling between the two amide-I and one amide-II vibrators should give rise to six sets of cross-peaks along the diagonal of the NR spectrum, as indicated by labels D, E, and F in Figure 5a$_2$. The fine structures observed here may be attributed to the overlapping of and interference between cross-peaks and/or to the presence of multiple conformers.

4.3. Resolving Power of the RPE Sequence. It has been shown previously that the NR sequence has a higher resolving power for closely spaced spectral features than the R sequence because nodal lines in the real and imaginary parts of the NR spectra are perpendicular to the diagonal.[9] Destructive interference in the overlapping region between vibrators can give rise to doublet features in the absolute magnitude NR spectra, whereas constructive interference in the overlapping region results in the elongation of the diagonal peak in the absolute magnitude R spectra. The manifestation of these effects was observed in the R and NR spectra of AcProND$_2$ in D$_2$O and attributed to the presence of two conformations whose amino amide-I frequencies are separated by less than the line width.[9]

For the RPE sequence, we performed model calculations to investigate its resolving power. The equations used in the calculations are described in detail in the Appendix. The results of our model calculations show that the RPE sequence also exhibits enhanced resolving power (Figure 9), similar to the NR sequence. This behavior happens because the RPE sequence shares similar nonrephasing properties in that the frequencies of the coherences involved in the T and t periods have the same sign (diagrams 7 and 8 in Figure 8c). The nodal line in the real part of RPE spectra intersects with the diagonal line at a sizable angle (Figure 9b), leading to destructive interference between the positive and negative peaks of nearby vibrators. Moreover, the RPE sequence resolves spectral features more clearly than the NR sequence (Figure 4c$_2$ and c$_3$) because the peaks in the RPE spectra are further separated along the ω_T dimension, and the diagonal profiles are not complicated by the presence of overlapping weak cross-peaks as in the NR spectra ($\mathscr{F}_b$ and $\mathscr{F}_g$ in Figure 8b).
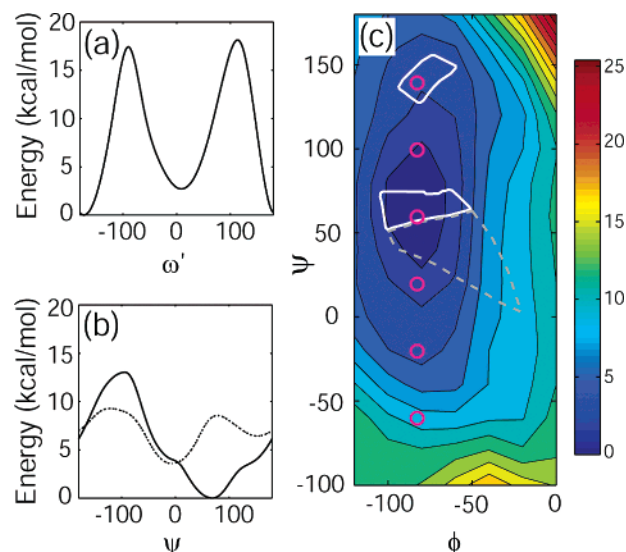

Figure 10. Potential energy surface (PES) of AcProNH$_2$ in vacuo calculated at the B3LYP/6-31+G(d,p) level. Optimized structures are obtained in 20° intervals. (a) The dihedral angle ω' scan shows two local minima that correspond to a trans and a cis conformer. (b) The PES scans along ψ, starting from the trans or the cis form show one minimum in the trans conformer (solid line) and ensure the presence of a stable cis conformer (dotted line). (c) The 2D PES of the trans conformer as a function of the (ϕ, ψ) dihedral angles. The global minimum at (ϕ, ψ) = (−83°, 69°) corresponds to the *trans*-C7 structure. The six circles indicate the dihedral angles of the six conformations employed in the 2D spectral simulations shown in Figure 12. The regions enclosed by the white solid and gray dashed lines indicate possible conformations that satisfy the transition dipole orientations obtained from ref 10. See Section 4.7 for details.

On the basis of the above discussion, we attribute the doublet features in Figure 4c$_2$ and c$_3$ to the presence of multiple conformations of AcProNH$_2$ in CDCl$_3$. The clearly resolved B′ and C′ peaks are assigned to the minor conformer. By line fitting the diagonal profile of Figure 4c$_3$, an area ratio of ∼3:1 was estimated between the two sets of peaks. Because the fitting was performed on the absolute magnitude spectrum instead of the real part and the same absorption cross sections for the two conformers were assumed, this ratio does not reflect the true population ratio of the two conformations. Nevertheless, this ratio is comparable to previous studies of a similar dipeptide AcProNHMe in CDCl$_3$, where a population ratio of ∼4:1 between the trans and cis conformations was determined.[5,18,20,58,59]

4.4. Conformational and Vibrational Analyses. To elucidate the multiple conformations of AcProNH$_2$, and to obtain molecular parameters for simulations of 2D IR spectra, we carried out ab initio calculations using the Gaussian 03 program package.[60] Previous RHF/6-31G* work on AcProNH$_2$ in vacuo found seven local minima; three of these minima are of the trans form, while the others are of the cis form.[6] We chose the most stable conformer as the starting point and calculated the potential energy surface (PES) as a function of the backbone dihedral angles in 20° intervals. Figure 10 illustrates the results of PES calculations in vacuo done at the B3LYP/6-31+G(d,p) level. Figure 10a shows a PES scan obtained by driving the dihedral angle ω'. The two local minima along ω' indicate the presence of a trans and a cis conformer. The following PES scans along ψ, starting from the trans or the cis form, confirm that the *trans*-C$_7$ structure is the most stable (Figure 10b, solid) and that a stable cis conformer does exist (Figure 10b, dotted). Figure 10c shows the 2D PES of the trans conformer as a function of two dihedral angles ϕ and ψ (105 structures). The global minimum at (−83°, 69°) corresponds to the C$_7$ structure,

TABLE 2: Optimized Structures and Vibrational Properties of AcProNH$_2$ in Vacuo and in Chloroform[a]

conformation	dihedral angle[b]	normal-mode frequency[c]			IR transition strength[d]			transition dipole angle[e]		
	$(\omega', \phi, \psi, \omega)$	ω_A	ω_B	ω_C	I_A	I_B	I_C	θ_{AB}	θ_{BC}	θ_{CA}
trans-C$_7$ [f]	(−173, −83, 69, −176)	1568	1635	1700	229	248	410	35 (30)	139 (129)	113 (134)
cis[f]	(10, −91, −6, 179)	1547	1669	1705	124	424	353	95 (60)	158 (164)	97 (133)
trans-C$_7$ [g]	(−172, −84, 65, −178)	1583	1636	1686	408	415	674	35 (34)	140 (127)	117 (133)
cis[g]	(9, −88, −10, −180)	1576	1657	1686	174	775	574	102 (62)	154 (161)	91 (133)

[a] Backbone dihedral angles, amide-I and -II normal mode frequencies, IR transition strengths, and relative angles between transition dipoles are obtained from DFT calculations and normal mode analysis at the B3LYP/6-311++G(d,p) level. [b] Defined in Figure 1; units in degrees. [c] Units in cm^{-1}. [d] Units in km/mol. [e] Units in degrees. Values in parentheses are calculated based on the local transition dipole model (see Section 4.4). [f] In vacuo. [g] In chloroform using SCRF−PCM.

somewhat different from (−80°, 87°) obtained at the HF/6-311++G(d,p) level in ref 11.

Further geometry optimization and normal-mode analysis were carried out for the *trans*-C$_7$ and cis forms at the B3LYP/6-311++G(d,p) level. The calculations were done in vacuo as well as in chloroform, using the self-consistent reaction field−polarizable continuum model (SCRF−PCM), as implemented in Gaussian 03. Table 2 shows the dihedral angles of the fully optimized structures and normal-mode frequencies. The dihedral angles of the structures in vacuo are very close to those reported for AcProNH$_2$ and AcProNHMe in previous theoretical studies[6,12,61,62] and only slightly deviate from those of the solvated structures. Also, the optimized structure, normal-mode frequencies, and the intensities of AcProNH$_2$ in vacuo at this level is essentially the same as those optimized at the B3LYP/6-31+G-(d,p) level in Figure 10. The amide-I and -II normal-mode frequencies of both conformers in Table 2 have been scaled by a factor 0.9701 and 0.9927 for the gas-phase and solvated structures, respectively. These factors were determined by least-squares fitting the three calculated *trans*-C$_7$ frequencies to the corresponding FT-IR peaks, considering that the C$_7$ conformer is the dominating species in the solution. The scaling factor for the gas-phase vibrational frequencies is very close to those obtained in other studies; 0.9679 with a similar basis set[63] or 0.97 with the same basis set.[64] The scaled transition frequencies for the solvated structure are within ±3.0 cm^{-1} of the experimental values. The vibrational frequencies for the amide-I bands of the trans form is lower than those of the cis form. This red-shift can be attributed to internal hydrogen bonding in the *trans*-C$_7$ conformer.

The calculated IR transition strengths are listed in Table 2. For both conformations, IR intensities of these three vibrators are within a factor of 2−3 of the FT-IR measurements (Section 3.1). However, the relative intensities of the three vibrators are quite different from the ratios between the experimental peak areas. This discrepancy cannot be resolved by taking into account a range of possible population weightings. It appears that IR intensities from DFT calculations are still not accurate enough for quantitative analysis even with the large basis set used here. This problem becomes even more severe in simulating 2D IR spectral intensities because they depend on transition dipole strength to the fourth power.

The relative angles between the amide-I and -II transition dipoles, θ_{ij}, are important factors that affect 2D IR spectra through their involvement in the $\langle \alpha_m \beta_n \gamma_u \delta_w \rangle$ terms (eqs 1−3). Table 2 lists these angles obtained directly from the normal-mode analysis performed on the gas-phase and solvated *trans*-C$_7$ and cis structures. The calculated angles θ_{AB}, θ_{BC}, and θ_{CA} of the solvated *trans*-C$_7$ conformer are 35°, 140°, and 117°, respectively. They agree well with the averaged experimental angles ∼35°, ∼130°, and ∼121° deduced from pump−probe anisotropy measurements of AcProNH$_2$ in CH$_2$Cl$_2$.[10] On the basis of these measurements, the authors of ref 10 concluded

that AcProNH$_2$ adopts the *trans*-C$_7$ structure, but we found that these angles could also represent other conformations of AcProNH$_2$, as we will discuss below in Section 4.7.

For weakly coupled vibrators, it seems reasonable to approximate the angle between the transition dipoles of two normal modes by that of two parent local modes because these normal modes are highly localized. Such a practice has been adopted in previous studies of AcProNH$_2$.[7,8,10,11,47] Also, the direction of the amino amide-II transition dipole was assumed to be along the C−NH$_2$ bond.[10,47] To test the validity of these approaches, we predicted θ_{ij} using our optimized structures by assuming the transition dipole of the amide-I mode to be 10° away from the C=O bond,[65] and that of the amide-II mode to be parallel to the C−NH$_2$ bond.[10,47] The angles from the local transition dipole model (listed inside the parentheses in Table 2) are quite different from those of the vibrational analysis. The main reason for the discrepancy results from the fact that the transition dipole of the amide-II normal mode intersects with the C−NH$_2$ bond at a large angle: 25° for the *trans*-C$_7$ structure and 48° for the cis conformer.

To further explore the dependence of relative transition dipole angles on peptide conformation, normal-mode analysis was performed on the same 105 trans structures from Figure 10c at the B3LYP/6-31+G(d,p) level. Parts a−c of Figure 11 show the contour maps of θ_{ij} as a function of (ϕ, ψ). Figure 11c indicates that the angle θ_{AC} between the amide-I and -II modes within the same peptide unit depends on the dihedral angles and hence is not a constant. In fact, the angle between the amide-II transition dipole and the C−NH$_2$ bond is found to range from 15° to 60° depending on the peptide conformation. This behavior confirms that the previous assumption of them being parallel is not adequate. In comparison to Figure 3b in ref 11, where the local transition dipole model was assumed, the θ_{BC} map between the two amide-I modes (Figure 11b) looks somewhat similar in trend, but on the average, their θ_{BC} values differ by ∼9° (room-mean-square difference). Although this difference seems small, an inaccurate map could give rise to quite different ϕ and ψ angles. We will further discuss the use of the θ_{ij} contour maps and the importance of obtaining the transition dipole orientation from quantum chemical calculations for each conformation in (ϕ, ψ) space in Section 4.7.

4.5. Coupling Constants, Local Mode Frequencies, and Anharmonicities. Although ab initio vibrational analysis provides two amide-I and one amide-II normal modes, we need to further extract information on the amide-I and -II local modes and coupling constants for 2D IR spectral simulations. To this end, we extended the Hessian matrix reconstruction method, carbonyl population analysis,[66] to include the amide-II mode. The amide-II local mode was represented by the ab initio eigenvector elements of the amino nitrogen and hydrogen atoms in the mass-weighted Cartesian coordinates, and the amide-I local mode was approximated by those of the carbonyl carbon and oxygen atoms. The 3-by-3 unitary transformation matrix,
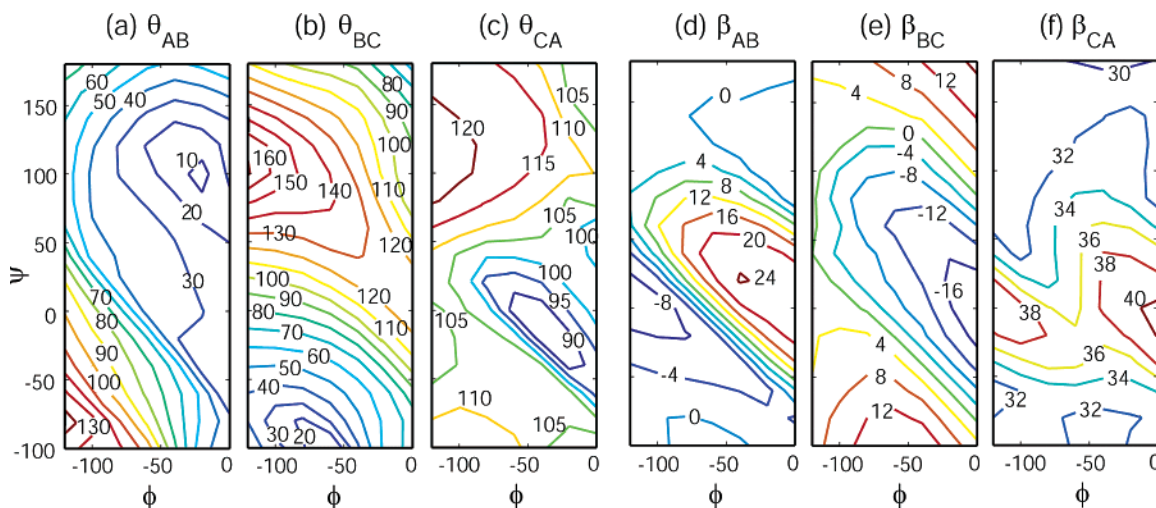
Figure 11. Conformational dependence of transition dipole orientations and coupling constants of the trans AcProNH$_2$ in vacuo as a function of the dihedral angles ϕ and ψ. Angles between transition dipoles [θ_{AB} (a), θ_{BC} (b), and θ_{CA} (c) in deg] were obtained from DFT calculations and normal-mode analyses at the B3LYP/6-31+G(d,p) level. Coupling constants [β_{AB} (d), β_{BC} (e), and β_{CA} (f) in wavenumbers] were calculated from an extended Hessian matrix reconstruction method.

TABLE 3: Local Mode Frequencies, Coupling Constants, Diagonal Anharmonicities, and Off-Diagonal Anharmonicities of AcProNH$_2$ in Chloroform (Units in cm^{-1})

conformation	local mode frequency			coupling constant			diagonal anharmonicity			off-diagonal anharmonicity		
	$\omega_A{}^0$	$\omega_B{}^0$	$\omega_C{}^0$	β_{AB}	β_{BC}	β_{CA}	Δ_{AA}	Δ_{BB}	Δ_{CC}	Δ_{AB}	Δ_{BC}	Δ_{CA}
trans-C$_7$	1599	1628	1678	±16.5	−4.7	±23.8	10.6	10.7	12.7	7.0	0.5	3.4
cis	1586	1655	1675	∓9.6	6.4	±30.6	12.4	14.1	12.1	1.4	0.5	4.6

U (matrix element U_{jJ}), between the normal modes ($J = A, B$, and C) and local modes ($j = a, b$, and c) was constructed. We assumed that the weight of the −NH$_2$ group in the Jth normal mode is proportional to $U_{aJ}{}^2$ by

$$U_{aJ}{}^2 = N_J \sum_{\substack{m=N,H \\ i=x,y,z}} u_{mi,J}{}^2$$

where $u_{mi,J}$ is the Jth eigenvector element of the nitrogen or hydrogen atoms of the amino group and the subscript i denotes the x, y, and z components. A positive sign was assigned to U_{aJ} if the ∠HNH bond angle of the a amide-II local mode increased during the Jth normal mode motion. The weight of the C=O group and signs of U_{bJ} and U_{cJ} were determined based on the same procedure used in ref 66. The **U** matrix thus obtained was used to reconstruct the Hessian matrix of local modes by the similarity transformation **H** = **U**Λ**U**$^{-1}$, where Λ is the eigenvalue matrix from the ab initio vibrational analysis. The resulting Hessian matrix was almost symmetrical. We enforced the symmetry of the Hessian matrix by taking the mean value of the upper and lower off-diagonal elements.

From Hessian matrix reconstruction, we obtained the local mode frequencies, $\omega_i{}^0$, and coupling constants, β_{ij}, for the *trans*-C$_7$ and cis conformers in chloroform, as listed in Table 3. The coupling constant β_{CA} that comes from amide-I and amide-II modes in the same peptide unit is ±23.8 cm^{-1} for the *trans*-C$_7$ form and ±30.6 cm^{-1} for the cis form. These values are comparable to experimental values of 27 cm^{-1} for NMA in DMSO[34] and ±31 cm^{-1} for AcProNH$_2$ in CH$_2$Cl$_2$.[10] The coupling constant β_{AB} (±16.5 cm^{-1} for the trans form), arising from amide-I and -II modes in different peptide units, shows a good agreement with that reported in ref 10 (±18.7 cm^{-1}). The coupling constant β_{CA} between amide-I modes (−4.7 cm^{-1} for the trans form) is close to the −4.9 cm^{-1} value calculated by Hahn et al.[11] but it is somewhat smaller than the experimental

estimate (±10 cm^{-1}) in ref 10. Parts d−f of Figure 11 show the conformational dependence of the coupling constants obtained from applying the Hessian matrix reconstruction method to the 105 gas-phase trans conformers.

To calculate the diagonal and off-diagonal anharmonicites for 2D spectral simulations, the local mode frequencies and the coupling constants were used to construct vibrational one- and two-exciton Hamiltonians.[67] Here a harmonic approximation was used, in which the part of the bilinear transfer matrix element between $v = 1$ and $v = 2$ states of individual vibrators is $\sqrt{2}$ times those for $v = 0$ to $v = 1$. The zero-order anharmonicities, Δ, of the amide-I and amide-II local modes were assumed to be the same because these modes have been shown to exhibit similar diagonal anharmonicities (Section 3.3 and ref 10). The one- and two-exciton normal modes were obtained from diagonalization of the Hamiltonians. The association between each normal mode and its parent local modes was established by identifying the eigenvector element that has the largest magnitude. Table 3 shows the resulting Δ_{ii} and Δ_{ij} of the amide-I and amide-II normal modes by setting $\Delta = 15.0$ cm^{-1} for the solvated structures. Here the value of Δ was chosen to yield the best fit of Δ_{ii} to the diagonal anharmonicity obtained from our pump−probe experiments (Section 3.3). For the *trans*-C$_7$ conformer, the amide-I/II mixed-mode anharmonicity of the amide modes within the same amide unit is found to be 3.5 cm^{-1}, in good agreement with the experimental value of 3.5 ± 0.5 cm^{-1} for NMA in DMSO[68] and 6.5 ± 1 cm^{-1} for AcProNH$_2$ in CH$_2$Cl$_2$,[10] and with the ab initio calculated value of 4.4 cm^{-1} for AcProNHMe in vacuo.[69] The mixed-mode anharmonicity of the amide-I and -II modes from different amide units has $\Delta_{AB} = 7.0$ cm^{-1}, very close to the 6.5 ± 1 cm^{-1} value determined for AcProNH$_2$ in CH$_2$Cl$_2$.[10] The two amide-I modes have an off-diagonal anharmonicity of $\Delta_{BC} = 0.5$ cm^{-1}, somewhat smaller than the measured value (1.5 ± 1 cm^{-1}) in CH$_2$Cl$_2$.[10] This is to be expected because the calculated β_{BC} is

Conformations of *N*-Acetyl-L-Prolinamide

J. Phys. Chem. B, Vol. 110, No. 40, 2006 **19901**

also smaller than the experimental estimates. On the basis of the second-order perturbation theory, the mixed-mode anharmonicity has a squared dependence on the associated coupling constant.[67]

It should be noted that there are two possible signs for β_{AB} and β_{CA} listed in Table 3. The signs in the top row correspond to the phase definition as described at the beginning of this section. Those in the bottom row correspond to the opposite definition, namely that a negative sign is assigned to U_{aJ} if the ∠HNH bond angle increases during the normal mode motion. This ambiguity in the sign does not affect the eigen frequencies of the one- and two-exciton bands. Hence the calculated diagonal and off-diagonal anharmonicities are independent of the sign.

4.6. Simulation of 2D IR Spectra. We used eqs 3 and A5−A10 to simulate the RPE spectra and the equations in ref 9 to simulate the R and NR spectra of AcProNH$_2$. These equations ignore dynamics due to coherence and population transfer between vibrational modes. This is a reasonable assumption in the present case because the measured energy transfer time ranges from 3 to >20 ps in CH$_2$Cl$_2$.[10] Because our laser pulses have a finite bandwidth, the response functions were convolved in the time domain with electric fields of the laser pulses represented by a Gaussian function. All time orderings of the pulses during pulse overlap were included.

Simulations of 2D IR spectra require a large number of input parameters. In ideal situations, all parameters could be determined experimentally. In reality, we need to make reasonable assumptions and simplifications. In the following discussion, we will briefly explain what assumptions were made, and how molecular parameters were determined.

We first considered two conformers, the *trans*-C$_7$ and cis forms, with a population ratio of 4:1 based on previous studies[5,18,20,58,59] and also on our RPE spectrum taken at (0, 0, 0, 0) polarization (Figure 4a$_3$ and c$_3$). For every vibrational mode, the transition dipole moment of each conformer was allowed to vary slightly from the value measured by linear FT-IR (Section 3.1), but the integrated vibrational intensity with population weighting was kept close to the experimental value. The diagonal and off-diagonal anharmonicities of both conformers were set to the values shown in Table 3. The fundamental frequencies, ω_A, ω_B, and ω_C, of the major conformer were set to within 3 cm^{-1} of the peak positions taken from the FT-IR measurements. Those of the minor conformer were chosen to best simulate the diagonal slices of the R and NR spectra at (0, 0, 0, 0) polarization (Figure 4c$_1$ and c$_2$).

We assumed that the vibrational dynamics of the two conformers were the same. The frequency fluctuations of the 0−1 and 1−2 transitions of the A, B, and C vibrators were considered to be strictly correlated and the correlation coefficients f_A, f_B, and f_C were set to 1. Assuming that the frequency fluctuations of the amide-I and -II modes were nearly uncorrelated to one another, we set the correlation coefficients c_{AB}, c_{BC}, and c_{CA} to 0. This assertion is consistent with previous experimental and theoretical studies of the alanine dipeptide that found the two amide-I bands of the peptide to be nearly uncorrelated.[39,70] The experimentally measured correlation coefficient between the amide-I and amide-II frequencies of NMA is also small.[34]

The population decay times of the three vibrators were set to the values obtained from the transient grating measurements (Figure 7). For the 0−1 transitions, the Lorentzian and Gaussian contributions to the pure dephasing rates Γ_A, Γ_B, Γ_C, σ_A, σ_B, and σ_C were allowed to vary. The diagonal anharmonicity was assumed to have no fast fluctuations ($\Gamma_{\Delta_i} = 0$) and no static inhomogeneity ($\sigma_{\Delta_i} = 0$). The decay of coherences during the *T* and *t* period due to finite lifetimes of the overtone and

combination bands were set to take the form of $(T_1^{i+i})^{-1} = 2(T_1^i)^{-1}$ and $(T_1^{i+j})^{-1} = (T_1^i)^{-1} + (T_1^j)^{-1}$, respectively, making our system approximate a harmonic oscillator linearly coupled to bath modes.[71−73]

Noting that the relative intensity ratio and the line shapes of the peaks in the R and NR spectra are very sensitive to the contributions of homogeneous and inhomogeneous broadening, we utilized the intensity ratios of A, B, and C peaks in the R and NR spectra (Figure 4a$_1$ and a$_2$) to determine the best Γ_i and σ_i parameters in a systematic way. Many Γ_i and σ_i pairs were first chosen from a grid of a (Γ_i, σ_i) map with a 1 cm^{-1} resolution using the criterion that each pair could produce a Voigt profile satisfying the linear FT-IR line width for each peak. This large set of parameters was used to calculate R and NR spectra, and only those pairs that could reproduce the measured peak intensity ratio between the R and NR spectra (∼1.4, ∼4, and ∼4 for peaks A, B, and C, respectively) were selected. Further refinement of the parameters was achieved by matching the calculated and experimental relative peak intensities in each 2D spectrum. Because the doublet features in the NR spectrum sensitively depend on the line widths and the peak positions of the minor conformer, the fundamental frequencies and line widths were fine-tuned iteratively to simulate the diagonal profiles of the R and NR spectra. The resulting parameters were used to simulate the RPE spectrum without further refinement. The simulated 2D (0, 0, 0, 0) spectra are shown in Figure 4b$_1$−b$_3$, and their diagonal slices (dashed blue) in Figure 4c$_1$−c$_3$. The parameters are: $\Gamma_A = 0.02$, $\Gamma_B = 3.7$, $\Gamma_C = 2.3$, $\sigma_A = 4.7$, $\sigma_B = 6.5$, and $\sigma_C = 7.0$ cm^{-1}. The fundamental frequencies of peaks A, B, and C are 1581, 1630, and 1686 cm^{-1} for the trans conformer, and 1591, 1645, and 1699 cm^{-1} for the minor conformer, respectively. The general features of the simulated 2D IR resemble these measurements quite well.

Simulations of the (45, −45, 90, 0) spectra using the same set of parameters are presented in Figure 5b$_1$−b$_3$. The relative intensities of the cross-peaks reasonably agree with the experimental data (Figure 5a$_1$−a$_3$) in their overall trends; E peaks are the most intense, D peaks show moderate intensity, and F peaks are the weakest. However, a closer comparison shows that the calculated intensity of the F peaks is much stronger than the experimental data suggested.

4.7. Conformations of AcProNH$_2$. To check whether a different major conformer may exist that provides a more quantitative agreement between the simulation and experiment, we carried out further simulations of 2D IR spectra using each trans structure in the (ϕ, ψ) space of Figure 10c as the major conformer. We focused on the (45, −45, 90, 0) cross-peaks because they are free from intense diagonal contributions. The simulation incorporated the relative transition dipole angles (Figure 11a−c) and off-diagonal anharmonicities of the amide-I and -II modes derived from the coupling constants (Figure 11d−f), as calculated in Sections 4.4 and 4.5. No other parameters were changed. Out of the 105 simulated spectra, those obtained at $\phi = -80°$ resemble the experimental data most closely. This is not unexpected because of the restriction on ϕ imposed by the pyrrolidine ring structure. Parts a−f of Figure 12 show six spectra in which the major trans conformations are indicated by the six circles (from bottom to top) in Figure 10c. These conformers are in the vicinity of (a) the α_R structure ($\psi \approx -50°$), (b) the crystal structure ($\psi = -14°$),[3] (c) the average conformation from MD simulation ($\psi = 15°$),[11] (d) the C$_7$ structure ($\psi \approx 70°$), (e) an intermediate conformation between C$_7$ and P$_{II}$, and (f) the P$_{II}$ conformation ($\psi \approx 150°$). As the dihedral angle ψ varies, changes in the cross-peak patterns are clearly seen. Figure 12d at $\psi = 60°$ shows a nearly identical cross-peak

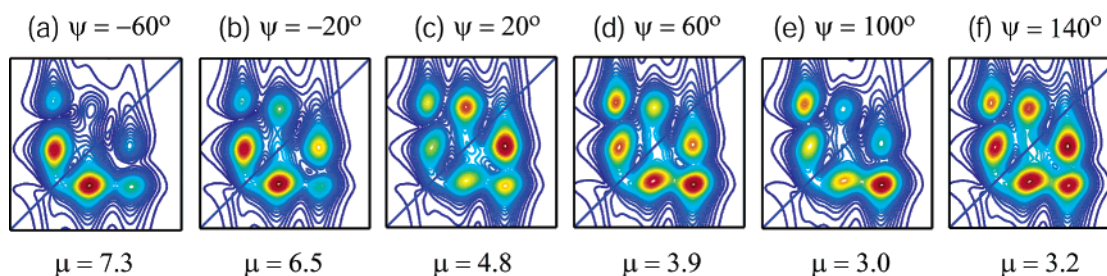$\mu = 7.3$ $\mu = 6.5$ $\mu = 4.8$ $\mu = 3.9$ $\mu = 3.0$ $\mu = 3.2$

Figure 12. Simulations of R spectra at (45, −45, 90, 0) polarization at a fixed dihedral angle $\phi = -80°$. Shown here are six representative ψ angles from −60° to 140° in 40° intervals; each spectrum is near (a) the α_R structure ($\psi \approx -50°$), (b) the crystal structure ($\psi = -14°$), (c) an average conformation from MD simulation ($\psi = 15°$), (d) the C7 structure ($\psi \approx 70°$), (e) an intermediate conformation between C_7 and P_{II}, and (f) the P_{II} conformation ($\psi \approx 150°$). Cross-peak patterns are distinct enough to specify the dihedral angle ψ. The simulated spectrum with $\psi = 100°$ (e) best reproduces the experimental cross-peak pattern in Figure 5a$_1$. The dipole moment μ below each figure is given in Debye. The frequency axes of these spectra span the same range as those in Figure 5a$_1$.

pattern to that in Figure 5b$_1$ which employs the solvated *trans*-C$_7$ structure as the major conformer. Among these spectra, the best matched cross-peak pattern to the experimental data (Figure 5a$_1$) occurs at $\psi = 100°$ (Figure 12e). This simulation result suggests that the ensemble averaged conformation of AcProNH$_2$ deviates from the *trans*-C$_7$ structure, the gas-phase global minimum, to an extended intermediate between C$_7$ and P$_{II}$ structures in CDCl$_3$.

To test the robustness of the above simulation procedure for structure determination, we extensively explored the dependence of the (45, −45, 90, 0) cross-peak patterns and the (0, 0, 0, 0) diagonal profiles on θ_{ij}, Δ_{ij}, Γ_i, and σ_i. It is found that the cross-peak patterns are very sensitive to θ_{ij} and Δ_{ij} but much less dependent on Γ_i and σ_i. On the contrary, the diagonal profiles exhibit the opposite sensitivity on these parameters. Judging from the quality of our systematic search for the best fit Γ_i and σ_i, we are confident that the validity of the major conformation determined here depends mainly on the accuracy of θ_{ij} and Δ_{ij}. Because we obtained θ_{ij} directly from ab initio normal-mode analysis, its accuracy is only determined by the level of quantum chemical calculations employed in this study. It is free from the inaccuracy inherent in the local mode transition dipole approximation used in previous studies. As discussed in Section 4.4, θ_{ij} obtained from this approximation can be quite different from that of normal-mode analysis. In fact, when we generated the 2D cross-peak patterns based on this approximation in our initial stage of simulations, we reached an erroneous conclusion that the best matched conformation has $(\phi, \psi) \approx (-120°, 120°)$, close to a parallel β-sheet structure. Thus, using the correct θ_{ij} maps in Figures 11a−c is critical for structure determination. The accuracy of Δ_{ij} is determined by the approximations involved in the Hessian matrix reconstruction method. As discussed in Section 4.5, the corresponding coupling constants β_{ij} are quite reasonable. Therefore, the structure, $(\phi, \psi) \approx (-80°, 100°)$, determined here should be representative of the trans conformation of AcProNH$_2$ in CDCl$_3$.

To understand how the solvent CDCl$_3$ influences the dominant conformation of AcProNH$_2$ compared to that in the gas phase, it is instructive to examine the gas-phase PES of the trans conformer in Figure 10c. It has a global minimum around $(\phi, \psi) = (-80°, 70°)$ with a valley elongated along the dihedral angle ψ. This indicates that angle ψ is rather flexible but angle ϕ is relatively rigid. The solvent could displace the global minimum along the vertical valley to a different ψ location with somewhat similar ϕ angle and/or stabilize shallow potential wells such as those in the solid curve of Figure 10b. In other words, in the presence of weakly polar CDCl$_3$, the potential energy landscape could be modified to favor other trans conformations and depopulate the C$_7$ conformation.

Previous CD, NMR, and IR studies on a closely related peptide AcProNHMe support this idea.[5,17,19,20] The population

of the *trans*-C$_7$ conformation decreases from 95% in tetrachloromethane (CCl$_4$)[17] to 80% in CDCl$_3$[5,20] and 60% in CD$_2$Cl$_2$.[19] The population of other conformations increases in more polar solvents. In CDCl$_3$ and dimethyl sulfoxide (CD$_3$SOCD$_3$), the P$_{II}$ conformation is increasingly populated, and the P$_{II}$ and α_R conformations seem to be equally populated with the C$_7$ structure in acetonitrile (CD$_3$CN).[5]

According to a long-established rule for solvent effects on molecular conformation, the conformation of the higher dipole moment will be preferentially stabilized in media of higher relative permittivity.[74] The calculated dipole moment of AcProNH$_2$, listed in Figure 12, decreases with increasing ψ. The rule would predict that the dominant conformation of AcProNH$_2$ shifts from C$_7$ toward α_R when it is solvated by weakly polar CDCl$_3$, but our results indicate an opposite shift toward P$_{II}$. In addition, previous studies suggest that trans AcProNH$_2$ takes the P$_{II}$ conformation in water, a very polar solvent.[2,13] The behavior of AcProNHMe in various solvents, as summarized above, does not follow this rule, either. The P$_{II}$ conformation is increasingly populated as solvent polarity increases. The dielectric constant of DMSO is higher than that of acetonitrile, but α_R is not observed in DMSO. These results suggest that the simple electrostatic consideration of molecular conformation is not sufficient for predicting solvent-dependent conformations for systems such as AcProNH$_2$ and AcProNHMe where specific solute/solvent interactions, such as hydrogen-bonding and steric hindrance, can play important roles. Although CDCl$_3$ has a low relative permittivity, experimental evidence has shown that CDCl$_3$ is capable of making hydrogen bonds with other molecules.[75] A recent MD simulation observed a weak hydrogen bond between CDCl$_3$ and the carbonyl of *N*-methylacetamide.[76] Thus, specific interactions between AcProNH$_2$ and CDCl$_3$ may affect its conformations.

Contrary to our results, a recent MD simulation of AcProNH$_2$ in CDCl$_3$ obtained a unimodal distribution of conformations with ensemble-averaged dihedral angles of $(\phi, \psi) = (-70°, 15°)$,[11] predicting a conformation shift from C$_7$ toward decreasing ψ, i.e., toward the crystal structure of AcProNH$_2$[3] and α_R. The discrepancy between their simulation and our experiment may come from the limitation of force field employed in their simulation. It has been shown that the AMBER program favors the α_R conformation but not an extended structure.[77]

Last, it is insightful to use our ab initio maps in Figure 11a−c to reinterpret the cross-peak anisotropy data of ref 10 by finding the (ϕ, ψ) coordinates where the contours of experimentally determined θ_{AB}, θ_{BC}, and θ_{CA} intersect. The two regions enclosed by the solid white lines in Figure 10c indicate the allowed (ϕ, ψ) coordinates for the major conformer when all possible experimental values were considered. This finding suggests that the major trans conformation of AcProNH$_2$ in CH$_2$-Cl$_2$ is either C$_7$ or P$_{II}$ or both. If we exclude the map in Figure

11c based on the usual assumption that θ_{CA} is independent of peptide conformation because it is the angle between the amide-I and -II modes within the same peptide unit, the region enclosed by the gray dashed line in Figure 10 also becomes allowed. Thus, utilizing the conformation dependence of all three angles in conformation analysis can greatly narrow down the allowed conformational space. The same analysis was performed on the $\theta_{AB'}$ and $\theta_{B'C}$ of a minor trans conformer reported in ref 10. We found a broadly allowed region centered at $(\phi, \psi) \approx (-95°, 105°)$, very different from their proposed α_R conformation. We also found that if the same conformation analysis was instead performed using the angle maps generated under the local mode transition dipole approximation, the resulting dihedral angles could differ by as much as $\sim30°$ depending on which definition of the transition dipole orientations in the literature[51,65] was used. These results demonstrate the importance of using angle maps from quantum-chemical calculations to guide experimental data interpretation.

5. Conclusions

In this study, we have shown that acquiring 2D IR spectra with multiple pulse sequences simultaneously at two polarization conditions can provide a substantial amount of structural information on a small peptide in solution. In particular, we have derived the major backbone structure of AcProNH$_2$ in CDCl$_3$ from its 2D IR spectra and discussed our findings in relationship with those from previous studies. In comparison to the recent applications of the 2D IR R sequence and transient pump–probe technique to the study of AcProNH$_2$, our combined experimental and simulation approaches offered distinct advantages. First, the multiple 2D spectra were utilized in a systematic way to extract the molecular parameters that these spectra are most sensitive to: obtaining vibrational frequencies and line widths from the peak positions and relative intensities of the $(0, 0, 0, 0)$ R and NR spectra, resolving trans and cis conformers by the $(0, 0, 0, 0)$ RPE and NR spectra and determining dihedral angles by simulating the $(45, -45, 90, 0)$ cross-peak patterns. This procedure circumvents the severe interference from the diagonal contributions encountered in previous studies and allows for quantitative determination of structure and dynamics.

Second, our approach involved extensive 2D IR spectral simulations for a large region of the Ramachandran space. Relative transition dipole angles, coupling constants, and mixed mode anharmonicities were obtained from normal-mode analysis, Hessian matrix reconstruction, and the vibrational exciton model, respectively. Obtaining these molecular parameters directly from quantum-chemical and semiempirical calculations is proven to be critical for structure determination.

The major trans conformation of AcProNH$_2$ in CDCl$_3$, determined by our 2D IR measurements, is an intermediate between the C$_7$ and the P$_{II}$ form centered at $(\phi, \psi) \approx (-80°, 100°)$. The effect of CDCl$_3$ on the conformations of AcProNH$_2$ does not follow the simple predictions based on solvent polarity. This suggests that specific peptide–solvent interactions may play an important role. In light of previous studies of AcProN-HMe using conventional spectroscopic techniques, another possible explanation of our results would be that trans AcProNH$_2$ adopts a bimodal distribution centered at the C$_7$ and P$_{II}$ structures with certain population weighting. To gain insight into the details of conformational distribution, higher-level MD simulations and quantum-chemical calculations that properly include solvent effects are needed to provide more accurate structures and molecular parameters for further simulations of 2D IR spectra. We hope that our results will stimulate further work in this direction.

Appendix: RPE Response Functions

To simulate 2D IR spectra, the dynamical factors $F(mn|qr|uw)$ in the response functions of eqs 1–3 need to be expressed in specific models. Here we describe the general expressions for the RPE sequence including the effects of vibrational frequency correlations. Corresponding factors for the R and NR sequences have been reported previously.[9] The vibrational dynamics of the system are modeled by assuming that the system–bath coupling is governed by stochastic processes that follow Gaussian statistics and neglecting the vibrational relaxation between level pairs. The population relaxation of the *i*th level is taken into account phenomenologically by a decay time of T_1^i. Applying cumulant expansion, the $F(mn|qr|uw)$ factors in eq 3 can be written as

$$F(i0|i+i,0|i0) = 2\mu_i^4 \exp\left[-\frac{\tau+t}{2T_1^i} - \frac{T}{2T_1^{i+i}} + g_{ii}(\tau) - \right.$$
$$g_{i\Delta_i}(\tau) - g_{ii}(T) + 2g_{i\Delta_i}(T) - g_{\Delta_i\Delta_i}(T) + g_{ii}(t) - g_{i\Delta_i}(t) -$$
$$g_{ii}(\tau+T) + g_{i\Delta_i}(\tau+T) - g_{ii}(T+t) +$$
$$\left. g_{i\Delta_i}(T+t) - g_{ii}(\tau+T+t)\right] \quad \text{(A1)}$$

$$F(i0|i+i,0|i+i,i) = F(i0|i+i,0|i0)\exp\left[-\frac{t}{2T_1^{i+i}} - \right.$$
$$g_{i\Delta_i}(T) + g_{\Delta_i\Delta_i}(T) - g_{i\Delta_i}(\tau+T) + g_{i\Delta_i}(T+t) -$$
$$\left. g_{\Delta_i\Delta_i}(T+t) + g_{i\Delta_i}(\tau+T+t)\right] \quad \text{(A2)}$$

$$F(i0|i+j,0|j0) = \mu_i^2\mu_j^2 \exp\left[-\frac{\tau}{2T_1^i} - \frac{T}{2T_1^{i+j}} - \frac{t}{2T_1^j} + \right.$$
$$g_{ij}(\tau) - g_{ij}(T) + g_{ij}(t) - g_{ii}(\tau+T) - g_{jj}(T+t) -$$
$$\left. g_{ij}(\tau+T+t)\right] \quad \text{(A3)}$$

$$F(i0|i+j,0|i0) = \mu_i^2\mu_j^2 \exp\left[-\frac{\tau+t}{2T_1^i} - \frac{T}{2T_1^{i+j}} + g_{ij}(\tau) - \right.$$
$$\left. g_{jj}(T) + g_{ij}(t) - g_{ij}(\tau+T) - g_{ij}(T+t) - g_{ii}(\tau+T+t)\right]$$
$$\text{(A4)}$$

$$F(i0|i+j,0|i+j,i) =$$
$$F(i0|i+j,0|j0)\exp\left[-\frac{t}{2T_1^{i+j}} - \frac{t}{2T_1^i} + \frac{t}{2T_1^j}\right] \quad \text{(A5)}$$

$$F(i0|i+j,0|i+j,j) =$$
$$F(i0|i+j,0|i0)\exp\left[-\frac{t}{2T_1^{i+j}} - \frac{t}{2T_1^j} + \frac{t}{2T_1^i}\right] \quad \text{(A6)}$$

Here the forbidden terms have been omitted. The line shape functions are generally defined as

$$g_{ab}(t) = \int_0^t d\tau_1 \int_0^{\tau_1} d\tau_2 \langle\delta\omega_a(\tau_2)\delta\omega_b(0)\rangle$$

where $\langle\delta\omega_a(\tau_2)\delta\omega_b(0)\rangle$ is the correlation function of the frequency fluctuations $\delta\omega_a(t)$ and $\delta\omega_b(t)$ about their mean values. The line shape functions included in this model are $g_{ii}(t)$, $g_{\Delta_i\Delta_i}(t)$, $g_{i\Delta_i}(t)$, and $g_{ij}(t)$, corresponding to autocorrelation functions $\langle\delta\omega_i(\tau_2)\delta\omega_i(0)\rangle$ and $\langle\delta\Delta_i(\tau_2)\delta\Delta_i(0)\rangle$ and cross-correlation functions $\langle\delta\omega_i(\tau_2)\delta\Delta_i(0)\rangle$ and $\langle\delta\omega_i(\tau_2)\delta\omega_j(0)\rangle$, respectively. The fluctuation in the off-diagonal anharmonicity, $\delta\Delta_{ij}(t)$, is not included.

In the case of a strict separation of time scales of homogeneous and inhomogeneous broadening, i.e., Bloch dynamics, the line shape functions $g_{ii}(t)$, $g_{\Delta_i\Delta_i}(t)$, $g_{i\Delta_i}(t)$, and $g_{ij}(t)$ become $[\Gamma_i t + (\sigma_i^2 t^2/2)]$, $[\Gamma_{\Delta_i}t + (\sigma_{\Delta_i}^2 t^2/2)]$, $f_i\sigma_i\sigma_{\Delta_i}t^2/2$, and $c_{ij}\sigma_i\sigma_j t^2/2$, respectively: Γ_i is the motionally narrowed pure dephasing rate of the $0-1$ transition for vibrator i, Γ_{Δ_i} characterizes the motionally narrowed part of the diagonal anharmonicity fluctuations, and σ_i and σ_{Δ_i} characterize the widths of the Gaussian inhomogeneous distributions of the $0-1$ transition and diagonal anharmonicity, respectively. The statistical correlation coefficients f_i and c_{ij} are defined as $\langle\delta\omega_i\cdot\delta\Delta_i\rangle/(\sigma_i\sigma_{\Delta_i})$, and $\langle\delta\omega_i\cdot\delta\omega_j\rangle/(\sigma_i\sigma_j)$, respectively. Under these assumptions, and setting τ to 0, the $F(mn|qr|uw)$ factors in eqs A1–A4 become

$$F(i0|i+i,0|i0) =$$
$$2\mu_i^4\exp\left[-\frac{T}{2T_1^{i+i}} - \frac{t}{2T_1^i} - \Gamma_i(4T+t) - \frac{1}{2}\sigma_i^2(2T+t)^2 - \Gamma_{\Delta_i}T - \frac{1}{2}\sigma_{\Delta_i}^2T^2 + f_i\sigma_i\sigma_{\Delta_i}(2T+t)T\right] \quad (A7)$$

$$F(i0|i+i,0|i+i,i) =$$
$$F(i0|i+i,0|i0)\exp\left[-\frac{t}{2T_1^{i+i}} - \Gamma_{\Delta_i}t - \frac{1}{2}\sigma_{\Delta_i}^2(2T+t)t + f_i\sigma_i\sigma_{\Delta_i}(2T+t)t\right] \quad (A8)$$

$$F(i0|i+j,0|j0) = \mu_i^2\mu_j^2\exp\left[-\left(\frac{1}{2T_1^{i+j}} + \Gamma_i + \Gamma_j\right)T - \left(\frac{1}{2T_1^j} + \Gamma_j\right)t - \frac{1}{2}\sigma_i^2T^2 - \frac{1}{2}\sigma_j^2(T+t)^2 - c_{ij}\sigma_i\sigma_jT(T+t)\right] \quad (A9)$$

$$F(i0|i+j,0|i0) = \mu_i^2\mu_j^2\exp\left[-\left(\frac{1}{2T_1^{i+j}} + \Gamma_i + \Gamma_j\right)T - \left(\frac{1}{2T_1^i} + \Gamma_i\right)t - \frac{1}{2}\sigma_j^2T^2 - \frac{1}{2}\sigma_i^2(T+t)^2 - c_{ij}\sigma_i\sigma_jT(T+t)\right] \quad (A10)$$

On the basis of these equations, it is clear that the vibrational dephasing of the two quantum coherences during the T period will be significantly faster than that of the single quantum coherences during the t period. For instance, eq A7 shows that the contribution of the pure dephasing rate Γ_i in T is 4 times that in t. In addition, these equations can be readily used to investigate the effects of vibrational frequency correlations on RPE spectra. If the frequency fluctuations of the two vibrators are correlated, the cross-peaks will be line-broadened. If the vibrators are anticorrelated, the cross-peaks will be line-narrowed, elongated toward the antidiagonal.

References and Notes

(1) Madison, V.; Schellman, J. *Biopolymers* **1970**, *9*, 511.
(2) Pogliani, L.; Ellenberger, M.; Valat, J.; Bellocq, A. M. *Int. J. Pept. Protein Res.* **1975**, *7*, 345.
(3) Benedetti, E.; Christensen, A.; Gilon, C.; Fuller, W.; Goodman, M. *Biopolymers* **1976**, *15*, 2523.
(4) Radding, W.; Ueyama, N.; Gilon, C.; Goodman, M. *Biopolymers* **1976**, *15*, 591.
(5) Madison, V.; Kopple, K. D. *J. Am. Chem. Soc.* **1980**, *102*, 4855.
(6) Ramek, M.; Kelterer, A. M.; Teppen, B. J.; Schafer, L. *J. Mol. Struct.* **1995**, *352*, 59.
(7) Zanni, M. T.; Gnanakaran, S.; Stenger, J.; Hochstrasser, R. M. *J. Phys. Chem. B* **2001**, *105*, 6520.
(8) Zanni, M. T.; Ge, N.-H.; Kim, Y. S.; Hochstrasser, R. M. *Proc. Natl. Acad. Sci. U.S.A.* **2001**, *98*, 11265.
(9) Ge, N.-H.; Zanni, M. T.; Hochstrasser, R. M. *J. Phys. Chem. A* **2002**, *106*, 962.
(10) Rubtsov, I. V.; Hochstrasser, R. M. *J. Phys. Chem. B* **2002**, *106*, 9165.
(11) Hahn, S.; Lee, H.; Cho, M. *J. Chem. Phys.* **2004**, *121*, 1849.
(12) Sahai, M. A.; Kehoe, T. A. K.; Koo, J. C. P.; Setiadi, D. H.; Chass, G. A.; Viskolcz, B.; Penke, B.; Pai, E. F.; Csizmadia, I. G. *J. Phys. Chem. A* **2005**, *109*, 2660.
(13) Lee, K.-K.; Hahn, S.; Oh, K.-I.; Choi, J. S.; Joo, C.; Lee, H.; Han, H.; Cho, M. *J. Phys. Chem. B* **2006**, http://dx.doi.org/10.1021/jp055846+.
(14) MacArthur, M. W.; Thornton, J. M. *J. Mol. Biol.* **1991**, *218*, 397.
(15) Brandts, J. F.; Halvorson, H. R.; Brennan, M. *Biochemistry* **1975**, *14*, 4953.
(16) Schmid, F. X.; Baldwin, R. L. *Proc. Natl. Acad. Sci. U.S.A.* **1978**, *75*, 4764.
(17) Madison, V.; Delaney, N. G. *Biopolymers* **1983**, *22*, 869.
(18) Higashijima, T.; Tasumi, M.; Miyazawa, T. *Biopolymers* **1977**, *16*, 1259.
(19) Liang, G.-B.; Rito, C. J.; Gellman, S. H. *Biopolymers* **1992**, *32*, 293.
(20) Akiyama, M.; Ohtani, T.; Furuta, Y.; Watanabe, E. *Spectrochim. Acta, Part A* **1994**, *50*, 1675.
(21) Hamm, P.; Lim, M. H.; Hochstrasser, R. M. *J. Phys. Chem. B* **1998**, *102*, 6123.
(22) Asplund, M. C.; Zanni, M. T.; Hochstrasser, R. M. *Proc. Natl. Acad. Sci. U.S.A.* **2000**, *97*, 8219.
(23) Golonzka, O.; Khalil, M.; Demirdöven, N.; Tokmakoff, A. *Phys. Rev. Lett.* **2001**, *86*, 2154.
(24) Asbury, J. B.; Steinel, T.; Stromberg, C.; Gaffney, K. J.; Piletic, I. R.; Goun, A.; Fayer, M. D. *Phys. Rev. Lett.* **2003**, *91*, 237402.
(25) Yeremenko, S.; Pschenichnikov, M. S.; Wiersma, D. A. *Chem. Phys. Lett.* **2003**, *369*, 107.
(26) Fulmer, E. C.; Ding, F.; Mukherjee, P.; Zanni, M. T. *Phys. Rev. Lett.* **2005**, *94*, 067402.
(27) Cowan, M. L.; Bruner, B. D.; Huse, N.; Dwyer, J. R.; Chugh, B.; Nibbering, E. T. J.; Elsaesser, T.; Miller, R. J. D. *Nature* **2005**, *434*, 199.
(28) Larsen, O. F. A.; Bodis, P.; Buma, W. J.; Hannam, J. S.; Leigh, D. A.; Woutersen, S. *Proc. Natl. Acad. Sci. U.S.A.* **2005**, *102*, 13378.
(29) Kurochkin, D. V.; Naraharisetty, S. R. G.; Rubtsov, I. V. *J. Phys. Chem. A* **2005**, *109*, 10799.
(30) Mukamel, S. *Annu. Rev. Phys. Chem.* **2000**, *51*, 691.
(31) Hamm, P.; Lim, M.; DeGrado, W. F.; Hochstrasser, R. M. *Proc. Natl. Acad. Sci. U.S.A.* **1999**, *96*, 2036.
(32) Woutersen, S.; Hamm, P. *J. Chem. Phys.* **2001**, *114*, 2727.
(33) Woutersen, S.; Mu, Y.; Stock, G.; Hamm, P. *Proc. Natl. Acad. Sci. U.S.A.* **2001**, *98*, 11254.
(34) Rubtsov, I. V.; Wang, J. P.; Hochstrasser, R. M. *Proc. Natl. Acad. Sci. U.S.A.* **2003**, *100*, 5601.
(35) Bredenbeck, J.; Helbing, J.; Behrendt, R.; Renner, C.; Moroder, L.; Wachtveitl, J.; Hamm, P. *J. Phys. Chem. B* **2003**, *107*, 8654.
(36) Volkov, V.; Hamm, P. *Biophys. J.* **2004**, *87*, 4213.
(37) Mukherjee, P.; Krummel, A. T.; Fulmer, E. C.; Kass, I.; Arkin, I. T.; Zanni, M. T. *J. Chem. Phys.* **2004**, *120*, 10215.
(38) Fang, C.; Hochstrasser, R. M. *J. Phys. Chem. B* **2005**, *109*, 18652.
(39) Kim, Y. S.; Wang, J. P.; Hochstrasser, R. M. *J. Phys. Chem. B* **2005**, *109*, 7511.
(40) Chung, H. S.; Khalil, M.; Tokmakoff, A. *J. Phys. Chem. B* **2004**, *108*, 15332.
(41) Maekawa, H.; Toniolo, C.; Moretto, A.; Broxterman, Q. B.; Ge, N.-H. *J. Phys. Chem. B* **2006**, *110*, 5834.
(42) Demirdöven, N.; Cheatum, C. M.; Chung, H. S.; Khalil, M.; Knoester, J.; Tokmakoff, A. *J. Am. Chem. Soc.* **2004**, *126*, 7981.
(43) Mukherjee, P.; Kass, I.; Arkin, I.; Zanni, M. T. *Proc. Natl. Acad. Sci. U.S.A.* **2006**, *103*, 3528.
(44) Wang, J. P.; Chen, J. X.; Hochstrasser, R. M. *J. Phys. Chem. B* **2006**, *110*, 7545.
(45) Smith, P. E.; Pettitt, B. M. *J. Phys. Chem.* **1993**, *97*, 6907.
(46) Bolhuis, P. G.; Dellago, C.; Chandler, D. *Proc. Natl. Acad. Sci. U.S.A.* **2000**, *97*, 5877.
(47) Karaiskaj, D.; Sul, S.; Jiang, Y.; Ge, N.-H. Resolving Conformations of Acetylproline-NH2 by Coherent 2D IR Spectroscopy. In *Ultrafast*

Phenomena XIV; Kobayashi, T., Okada, T., Kobayashi, T., Nelson, K. A., De Silvestri, S., Eds.; Springer-Verlag: Berlin, 2005; p 545.

(48) Hamm, P.; Kaindl, R. A.; Stenger, J. *Opt. Lett.* **2000**, *25*, 1798.

(49) Zhang, W. M.; Chernyak, V.; Mukamel, S. *J. Chem. Phys.* **1999**, *110*, 5011.

(50) Scheurer, C.; Mukamel, S. *J. Chem. Phys.* **2001**, *115*, 4989.

(51) Torii, H.; Tasumi, M. *J. Chem. Phys.* **1992**, *96*, 3379.

(52) Venkatramani, R.; Mukamel, S. *J. Chem. Phys.* **2002**, *117*, 11089.

(53) Fulmer, E. C.; Mukherjee, P.; Krummel, A. T.; Zanni, M. T. *J. Chem. Phys.* **2004**, *120*, 8067.

(54) Hochstrasser, R. M. *Chem. Phys.* **2001**, *266*, 273.

(55) Golonzka, O.; Tokmakoff, A. *J. Chem. Phys.* **2001**, *115*, 297.

(56) Zhuang, W.; Abramavicius, D.; Mukamel, S. *Proc. Natl. Acad. Sci. U.S.A.* **2005**, *102*, 7443.

(57) Krummel, A. T.; Mukherjee, P.; Zanni, M. T. *J. Phys. Chem. B* **2003**, *107*, 9165.

(58) Beausoleil, E.; Lubell, W. D. *J. Am. Chem. Soc.* **1996**, *118*, 12902.

(59) Jhon, J. S.; Kang, Y. K. *J. Phys. Chem. A* **1999**, *103*, 5436.

(60) Frisch, M. J.; Trucks, G. W.; Schlegel, H. B.; Scuseria, G. E.; Robb, M. A.; Cheeseman, J. R.; Montgomery, J. A., Jr.; Vreven, T.; Kudin, K. N.; Burant, J. C.; Millam, J. M.; Iyengar, S. S.; Tomasi, J.; Barone, V.; Mennucci, B.; Cossi, M.; Scalmani, G.; Rega, N.; Petersson, G. A.; Nakatsuji, H.; Hada, M.; Ehara, M.; Toyota, K.; Fukuda, R.; Hasegawa, J.; Ishida, M.; Nakajima, T.; Honda, Y.; Kitao, O.; Nakai, H.; Klene, M.; Li, X.; Knox, J. E.; Hratchian, H. P.; Cross, J. B.; Bakken, V.; Adamo, C.; Jaramillo, J.; Gomperts, R.; Stratmann, R. E.; Yazyev, O.; Austin, A. J.; Cammi, R.; Pomelli, C.; Ochterski, J. W.; Ayala, P. Y.; Morokuma, K.; Voth, G. A.; Salvador, P.; Dannenberg, J. J.; Zakrzewski, V. G.; Dapprich, S.; Daniels, A. D.; Strain, M. C.; Farkas, O.; Malick, D. K.; Rabuck, A. D.; Raghavachari, K.; Foresman, J. B.; Ortiz, J. V.; Cui, Q.; Baboul, A. G.; Clifford, S.; Cioslowski, J.; Stefanov, B. B.; Liu, G.; Liashenko, A.; Piskorz, P.; Komaromi, I.; Martin, R. L.; Fox, D. J.; Keith, T.; Al-Laham,

M. A.; Peng, C. Y.; Nanayakkara, A.; Challacombe, M.; Gill, P. M. W.; Johnson, B.; Chen, W.; Wong, M. W.; Gonzalez, C.; Pople, J. A. *Gaussian 03*; Gaussian, Inc.: Wallingford, CT, 2004.

(61) Kang, Y. K. *J. Phys. Chem.* **1996**, *100*, 11589.

(62) Kang, Y. K. *J. Mol. Struct. (THEOCHEM)* **2002**, *585*, 209.

(63) Andersson, M. P.; Uvdal, P. *J. Phys. Chem. A* **2005**, *109*, 2937.

(64) Garbuzova, I. A.; Lokshin, B. V. *Russ. Chem. Bull.* **2004**, *53*, 1894.

(65) Torii, H.; Tasumi, M. *J. Raman Spectrosc.* **1998**, *29*, 81.

(66) Ham, S.; Cha, S.; Choi, J.-H.; Cho, M. *J. Chem. Phys.* **2003**, *119*, 1451.

(67) Hamm, P.; Hochstrasser, R. M. Structure and Dynamics of Proteins and Peptides: Femtosecond Two-Dimensional Infrared Spectroscopy. In *Ultrafast Infared and Raman Spectroscopy*; Fayer, M. D., Ed.; Marcel Dekker Inc.: New York, 2001; p 273.

(68) Rubtsov, I. V.; Kumar, K.; Hochstrasser, R. M. *Chem. Phys. Lett.* **2005**, *402*, 439.

(69) Wang, J. P.; Hochstrasser, R. M. *J. Phys. Chem. B* **2006**, *110*, 3798.

(70) Gnanakaran, S.; Hochstrasser, R. M. *J. Am. Chem. Soc.* **2001**, *123*, 12886.

(71) Owrutsky, J. C.; Raftery, D.; Hochstrasser, R. M. *Annu. Rev. Phys. Chem.* **1994**, *45*, 519.

(72) Oxtoby, D. W. *Adv. Chem. Phys.* **1981**, *47*, 487.

(73) Tominaga, K.; Yoshihara, K. *J. Phys. Chem. A* **1998**, *102*, 4222.

(74) Reichardt, C. *Solvents and Solvent Effects in Organic Chemistry*, 3rd ed., updated and enlarged; Wiley-VCH: Weinheim, 2003; pp 126−132.

(75) Pimentel, G. C.; McClellan, A. L. *The Hydrogen Bond*; W. H. Freeman: San Francisco, 1960.

(76) DeCamp, M. F.; DeFlores, L.; McCracken, J. M.; Tokmakoff, A.; Kwac, K.; Cho, M. *J. Phys. Chem. B* **2005**, *109*, 11016.

(77) Hu, H.; Elstner, M.; Hermans, J. *Proteins* **2003**, *50*, 451.